MATERIALS CHEMISTRY
FRONTIERS

Accepted Manuscript

This article can be cited before page numbers have been issued, to do this please use: F. A. Sater, B. Bouvet, S. Sene, G. Félix, E. Adriaenssens, J. Joly, G. Audran, S. R. A. Marque, J. Larionova and Y. Guari, *Mater. Chem. Front.*, 2025, DOI: 10.1039/D4QM01022A.

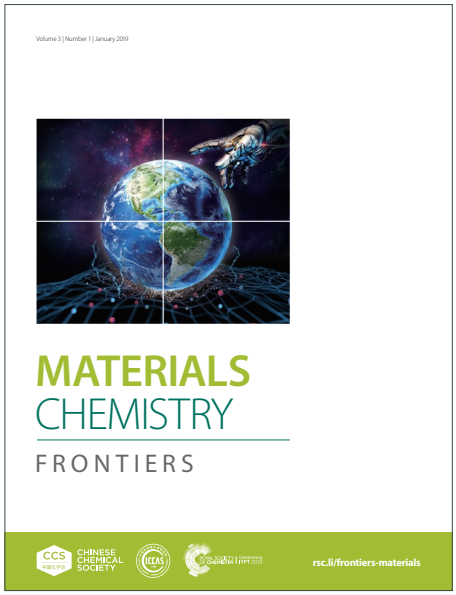

View Article Online
DOI: 10.1039/D4QM01022A

ARTICLE

Controlled Radical Release with Iron Oxide Nanoparticles Grafted with Thermosensitive Alkoxyamine Triggered by External *Stimuli*

Received 00th January 20xx,
Accepted 00th January 20xx

DOI: 10.1039/x0xx00000x

Farah Abdel Sater,[a£] Basile Bouvet,[a£] Saad Sene,[a] Gautier Félix,[a] Erwan Adriaenssens,[b] Jean-Patrick Joly,[b] Gerard Audran,[*b] Sylvain R. A. Marque,[*b] Joulia Larionova[*a] and Yannick Guari[a]

We report an investigation of a controlled radical release produced by iron oxide nanoparticles (IONP) of *ca.* 25 nm covalently grafted through phosphonic groups with a thermosensitive alkoxyamine, 6-(4-(1-((di-tert-butylamino)oxy)ethyl)benzamido)hexyl)phosphonic acid having a relatively low homolysis temperature (k_d = 6.4·10^{-4} s^{-1} at 77 °C, E_a = 117.8 kJ.mol^{-1}). Action of an alternating current magnetic field (AMF) or a light irradiation at 808 nm produces a rapid heating of the nanoparticles' surface, which induces the homolysis of the C-ON bond of alkoxyamines providing the efficient formation of free radicals. The kinetic of homolysis investigated by Electronic Paramagnetic Resonance (EPR) spectroscopy indicates that light irradiation at 808 nm (2.6 W·cm^{-2}) enabled efficient radical release from grafted nanoparticles at 44 °C ($t_{1/2}$ = 23.6 min), whereas the free molecule required 20 h to reach the same conversion at this temperature. AMF exposure accelerates the homolysis of alkoxyamine-grafted nanoparticles (16 kA·m^{-1}, 2.9 mg.mL^{-1}) twofold compared to the free alkoxyamine at 77 °C ($t_{1/2}$ = 7.9 min *vs* 18 min). These findings underscore the critical importance of localized nanoscale effects, demonstrating that the homolysis rate at the nanoparticle surface under external *stimuli* is significantly higher compared to external solution heating, with this enhancement being even more pronounced under light irradiation.

Introduction

Multifunctional nano-objects, capable of initiating controlled multi-step processes remotely activated by an action of external *stimuli*, have garnered a great deal of attention in the recent years due to their application in the field of biology and medicine for controlled delivery of drugs, radicals, nucleic acids, siRNA or genes,[1–5] but also for enzymatic regulation,[6] separation,[7] catalysis,[8] controlled polymerization,[9] sensing,[8] etc. These intricate systems commonly contain inorganic nanoparticles acting as magnetothermal or photothermal nano-heaters combined with thermosensitive shells or matrixes (such as polymers, liposomes, organic molecules) containing incorporated or attached payload. When subjected to the remote action of a light irradiation (photothermal activation) or an alternating magnetic field (AMF) (magnetic stimulation), these nanoparticles generate localised temperature rise near their surface, which, in turn, activates the transformation of thermosensitive moieties and therefore delivery of a payload. This so-called cascade multi-step strategy excels over the conventional single-functional approach, demonstrating superior controllability, specificity, efficiency of actions and often synergistic effects.

Among different inorganic nano-objects used as remotely activated nano-heaters, iron oxide nanoparticles (IONP) are the mostly investigated in the literature since their composition, size, morphology, surface state and therefore their heating properties can be precisely controlled.[10] Indeed, they can efficiently convert electromagnetic energy into heat upon exposure to AMF in the 100-350 kHz radiofrequency range with a few tens of kA.m^{-1} field intensity.[11] While investigated for numerous decades, the recent years have witnessed extensive development of a new generation of magnetic IONP with various morphologies, featuring improved magnetic properties, making them efficient as magnetothermal nano-heaters with high specific absorption rates (SAR) values.[12–16] Moreover, IONP have recently been investigated also as rather interesting photothermal agents within the near-infrared (NIR) window, as they effectively convert light into thermal energy.[17,18]

Of the various employment of smart nano-systems involving multistep processes, the controlled release of radical and/or Reactive Oxygen Species (ROS) triggered by photothermal, magnetothermal, enzyme and other actions, holds particular promise in biomedical area and materials science.[19–23] On one hand, it presents unique advantages for biomedical applications over classical drugs delivery due to selective and very local cytotoxicity, capitalizing on the inherent ability of radicals to induce targeted damage to cancer cells or bacteria while sparing normal tissues. Additionally, the mechanisms of action differ significantly from traditional drugs and show promising

[a] ICGM, Univ. Montpellier, CNRS, ENSCM, CNRS Montpellier, France, E-mail : joulia.larionova@umontpellier.fr, yannick.guari@umontpellier.fr
[b] Aix Marseille Univ, CNRS, ICR, UMR 7273, Avenue Escadrille Normandie-Niemen, 13397 Marseille CEDEX 20, France. E-mail : g.audran@univ-amu.fr, sylvain.marque@univ-amu.fr
[£] These authors equally contributed to this work
Supplementary Information available: [details of any supplementary information available should be included here]. See DOI: 10.1039/x0xx00000x

strategies to overcome challenges associated with drug resistance. Moreover, the combination of remotely activated heating and radicals' delivery introduces synergistic effects, creating a dynamic interplay that elevates the overall efficiency and specificity of the therapeutic action. On the other hand, some of these systems enable nanoparticle-assisted controlled radical polymerization, offering the creation of intricate polymer-based materials.[9,24,25] This method can be especially beneficial in situations where classical radical polymerization methods falter including the employment of highly reactive monomers, requirements for precise control over surface functionalization, the challenging design of complex polymer architectures, and the synthesis of intricate hybrid materials. The literature analysis indicates that the majority of systems offering the nanoparticles-assisted delivery of radicals/ROS involves the presence of oxygen-rich environments. However, the generation of oxygen-independent free radicals offers a pivotal advantage in various scenarios, including the hypoxic conditions prevalent in tumours, some environmental remediations or industrial polymerization reactions. In this regard, an intense research activity has been developed over the past few years, based on a strategy combining an alkyl radical generator with an organic[26] or inorganic nano-heater.[27] Among these, there are notably oxide nanoparticles (iron oxides,[28] MnO_2[29]), sulphides (Bi_2S_3,[30] CuS,[31] $CuFeS_2$,[32] FeS_2,[33] Ag_2S[34,35]) or carbides (Fe_5C_2,[36] Nb_2C,[37]), metals (Au,[38] PdAu,[39]) and Prussian blue[40] for which the temperature elevation is triggered either by light irradiation or application of an alternating magnetic field. This stimuli-induced heat generation leads to the activation of the radical generator which, with exceptions of peroxymonosulfate or peroxydisulfate salts,[31,41] is 2,2'-azobis-[2-(2-imidazolin-2-yl)propane] dihydrochloride (AIPH) possessing a thermosensitive azo function, thereby inducing the oxygen-independent release of alkyl radicals through a cascade process. To the best of our knowledge, IONP have been relatively scarcely investigated to design nano-systems able to radicals' delivery in a multistep cascade fashion, where each step is regulated by a specific parameter. We can cite for instance a few works where AIPH have been inserted into the porous IONP of 184 nm[28] or co-loaded with small spherical 10 nm IONP into large polymer nanoparticles.[42] Note however, that in these works, the radical initiators were simply inserted and not covalently linked to the hosting nanoparticles, leaving some inconvenient or risks compromising efficiency, including possible molecules' leaching into the surrounding environment, limited stability over time, the limited precision in efficiency to trigger mechanisms, etc.

Alkoxyamines present an interesting alternative to AIPH or sulphate derivatives as a source of radicals. Indeed, these organic molecules of the general formula $R_1R_2NOR_3$ possess homolysable C-ON bond, which can be cleaved upon an activation, generating therefore two radical species, alkyl ($\bullet R_3$) and nitroxyl ($R_1R_2NO\bullet$).[43] They offer unique advantages, including tunable activation energy and important stability. Various types of the C-ON bond activation for free alkoxyamine molecules have been investigated, including chemical activation, light irradiation or thermal heating.[44] The lability of the C-ON bond in alkoxyamines depends on different factors,[45–47] which can be modulated to create stable alkoxyamine molecules with adjustable activation energy and, therefore, tuneable homolysis temperatures.[43] Moreover, alkoxyamines can be functionalized with specific moieties enable to coordinate the surface of nanoparticles.

Recently, we reported the first example of magnetic IONP of *ca*. 25 nm covalently grafted with a thermosensitive radical initiator alkoxyamine, (6-{4-[1-(2,2,6,6-tetramethyl-piperidin-1-yloxy)-ethyl]benzoylamino}-hexyl)-phosphonate.[48] These nanoparticles were able to provide a controlled delivery of radicals in *tert*-butylbenzene at around 100 °C remotely triggered by an application of AMF. Encouraged by these promising results, we extended our investigations to another alkoxyamine derivative, (6-(4-(1-((di-tert-butylamino)oxy)ethyl)benzamido)hexyl) phosphonic acid, which is expected to exhibit a lower activation energy barrier and, consequently, significantly reduced homolysis temperature.

In this article, we report on design of new nano-objects consisting of IONP covalently grafted with (6-(4-(1-((di-tertbutylamino)oxy)ethyl)benzamido)hexyl) phosphonate and investigations of their radical release ability under external *stimuli*. Alongside investigation of magnetothermal activation of our system in different conditions (nanoparticle concentration, AMF parameters, solvents), we also focused on exploring photothermal triggering under light irradiation at 808 nm. The kinetic of homolysis investigated by Electronic Paramagnetic Resonance (EPR) spectroscopy indicates that light irradiation at 808 nm (2.6 $W \cdot cm^{-2}$) enabled efficient radical release from grafted nanoparticles at 44 °C ($t_{1/2}$ = 23.6 min), whereas the free molecule required 20 h to reach the same conversion at this temperature. AMF exposure accelerates the homolysis of alkoxyamine-grafted nanoparticles (16 $kA \cdot m^{-1}$, 2.9 $mgmL^{-1}$) twofold compared to the free alkoxyamine at 77 °C ($t_{1/2}$ = 7.9 min *vs* 18 min). Our results highlight the critical importance of localized nanoscale effects, demonstrating that the homolysis rate at the nanoparticle surface under external *stimuli* is significantly higher compared to bulk solution heating, with this enhancement being even more pronounced under light irradiation.

Results and discussion

Synthesis and characterisations

The synthesis of new IONP@alkoxyamine nanoparticles was performed in three steps: (*i*) the synthesis of an alkoxyamine derivative containing both, di-tert-butyl-nitroxide group with thermosensitive C-ON bond and pending phosphonic acid moiety able to coordinate Fe^{2+}/Fe^{3+} ions on the nanoparticles' surface, (*ii*) the synthesis of the pristine IONP, (*iii*) the grafting of the alkoxyamine through the coordination of the phosphonic acid groups to the IONP's surface.

First, the synthesis of the alkoxyamine derivative was performed following a five-step procedure starting from the commercially available para-vinyl benzoic acid, which was

esterified with methyl iodide (see Experimental Part). Then, the ester was coupled with di-tert-butyl-nitroxide radical using the Jacobsen's catalyst. The corresponding ester-alkoxyamine was hydrolysed into the carboxylic derivative, which is transformed in diethyl(6-(4-(1-((di-tert-butylamino)oxy)ethyl) benzamido) hexyl) phosphonate. The final step consists in hydrolysis of the phosphonate group into (6-(4-(1-((di-tert-butylamino)oxy) ethyl)benzamido)hexyl)phosphonic acid. All intermediate products, as well as the final alkoxyamine molecule were characterized by NMR (^{1}H and ^{31}P) (Fig. S1 – S5, ESI) and HRMS. The pristine IONP stabilized by oleyl acid and oleylamine (IONP/OA/OL) were prepared by flash thermolysis method using FeO(OH) precursor in *n*-docosane with an additional oxidation step (FeO into Fe_3O_4) as previously reported.[48] Finally, the post synthetic covalent grafting of the alkoxyamine derivative (6-(4-(1-((di-tert-butylamino)oxy)ethyl)benzamido)hexyl) phosphonic acid to the surface of IONP/OA/OL was performed by coordination of its phosphonate groups to Fe^{2+}/Fe^{3+} ions of the IONP's surface (Fig. 1).

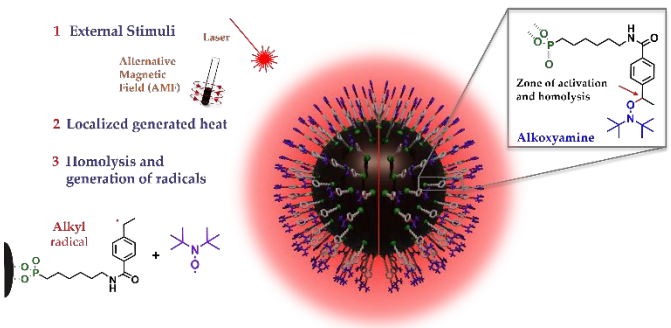

Figure 1. Schematic representation of IONP@alkoxyamine nano-objects providing a controlled radical release triggered by external *stimuli* (AMF or light irradiation) in a cascade action.

Transmission Electronic Microscopy (TEM) images of IONP/OA/OL and IONP@alkoxyamine nanoparticles are shown in Fig. 2 a, b. They indicate that the spherical morphology of the IONP was not impacted by the alkoxyamine's grafting. Their size distributions are equal to 25.08 ± 1.61 and to 25.50 ± 1.90 nm respectively (Fig. S6, ESI). The dynamic light scattering (DLS) analysis demonstrates the fact that the obtained nanoparticles are well dispersed and not aggregated (Fig. S7, ESI).

The Scanning Electron Microscopy (SEM) coupled with EDX analysis permitted to determine for the synthesized IONP@alkoxyamine nanoparticles the Fe/P ratio = 98.4/1.6, which indicates the successful grafting of the alkoxyamines to the nanoparticles' surface. It permits to estimate that there are 2.6 phosphorus atom per nm^2 of IONP. The successful grafting has been confirmed by infrared (IR) spectroscopy through the appearance of the alkoxyamine-related bands in the IR spectrum of the IONP@alkoxyamine nanoparticles when compared with the one of IONP/OA/OL and the free alkoxyamine molecule (Fig. S8, ESI). The IR spectrum of IONP@alkoxyamine shows the appearance of the stretching vibration of P-O-Fe bond at 1027 cm^{-1} attesting the successful coordination of the phosphonate groups to iron ions of the surface. Moreover, ν(C=O) at 1633 cm^{-1} of the alkoxyamine can also be found. The characteristic ν(Fe-O) vibrations of iron oxide is still present at 564 cm^{-1}. The powder X-Ray diffraction (PXRD) patterns of the obtained IONP@alkoxyamine nanoparticles (Fig. S9, ESI) show the reflections, which could be attributed to the main Fe_3O_4 phase, while the minor presence of FeO or even γ-Fe_2O_3 phases cannot be excluded.[49–51] The calculated lattice constant is equal to 8.38 Å, which is in accordance to the main magnetite phase 8.39 Å (JCPDS 19-629). The crystalline domain was calculated from the Scherrer formula giving an average value of *ca*. 22.4 nm.

The magnetic properties of the pristine IONP and IONP@alkoxyamine nanoparticles were investigated in powdered samples using SQUID-MPMS magnetometer working in the 1.8 – 350 K temperature range up to 7 T. The field dependences of the magnetization performed at 300 K for both samples are shown in Fig. S10a (ESI). The values of the saturation magnetization is equal of 62 Am^2.Kg^{-1} for both samples (before and after alkoxyamine grafting), which is lower in comparison to the value observed for the bulk pure magnetite (80 A.m^2.Kg^{-1}).[52] This is currently observed for IONP nanoparticles and can be explained by the presence of other phases besides magnetite with lower magnetization values (initial non oxidized FeO, which is diamagnetic and overoxidized γ-Fe_2O_3, as well as by the possible occurrence of spin frustration at the nanoparticles' surface.[49,50,53] Note that the value of the saturation magnetization is not changed after the alkoxyamine's grafting. The coercive fields at 300 K are equal to 2.2 and 13.6 mT for IONP and IONP@alkoxyamine, respectively. The temperature dependence of the magnetization performed in Zero Field Cooled (ZFC)/Field Cooled (FC) modes under an applied static magnetic field of 100 Oe present similar allure for both samples, which are typical for the IONP nanoparticles of *ca*. 25 nm with the main magnetite phase (Fig. S10b and S10c, ESI). The blocking/freezing temperature determined as the maximum on the ZFC curve is situated at 371 K for the pristine IONP, while it is above 400 K for IONP@alkoxyamine nanoparticles. This result may be explained by the covalent alkoxyamine grafting on the surface of the IONP, which visibly helps to remove the surface spin frustration usually occurring for IONP.

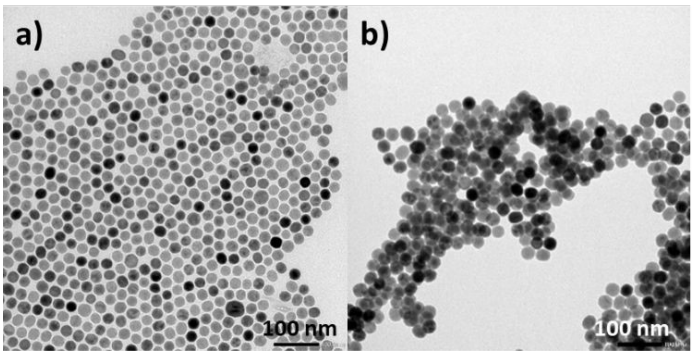

Figure 2. TEM images of: (a) the pristine IONP/OA/OL nanoparticles, (b) the IONP@alkoxyamine nanoparticles.

View Article Online
DOI: 10.1039/D4QM01022A

Magnetothermal and photothermal heating

The magneto- and photothermal properties of IONP@alkoxyamine nanoparticles were investigated to demonstrate their heating abilities triggered by either AMF or light irradiation.

Magnetothermal properties. The macroscopic heating of IONP@alkoxyamine nanoparticles was remotely activated by using AMF of 340 kHz and 20 mT (16 kA.m^{-1}). Thermal camera or optical fibre, which provided similar results, were used for temperature monitoring. First of all, the temperature elevation as a function of time was investigated for colloidal solutions of different concentrations varying from 0.1 to 4 mg mL^{-1} in *tert*-butylbenzene (Fig. 3). The *tert*-butylbenzene without nanoparticles was used as a reference. It did not provide any temperature elevation when submitted to the action of the magnetic field in the same conditions. On the contrary, the colloidal solutions containing IONP@alkoxyamine nanoparticles induce a rapid temperature rise. On the *T vs time* curves one can see a linear zone in the first 2 min of the AMF application and then a tendency to saturation (Fig. 3a). As an example, the temperature of 77 °C is reached after 10 min of exposure for the colloidal solution of 4 mg.mL^{-1}. Note that for all concentrations the temperature remains quasi constant after 10 min when the magnetic field is maintained. Fig. 3b illustrates the variation of ΔT as a function of nanoparticles' concentration. ΔT is determined here by subtracting the initial temperature from the temperature recorded after 10 minutes of AMF exposure. As shown, ΔT increases in a linear fashion with rising nanoparticle concentration. This indicates that the influence of dipolar nanoparticle interactions is not predominant at the concentrations under consideration.[54]

The SAR value is used to evaluate the magnetothermal performance of magnetic nanoparticles by quantifying the generated heat power under applied AMF.[11] The estimation of the SAR value was performed by fitting of the whole *T vs time* curves with a phenomenological model, incorporating a thermal exchange function developed with the second order Taylor series (see ESI for details).[55,56] The best fit provided the average SAR value (per g of nanoparticles) of 205±1 W.g^{-1} (Fig. 3). The corresponding intrinsic loss power (ILP) value, which permits the comparison of the heating capacity of nanoparticles regardless of the alternating magnetic field amplitude and frequency[11], is equal to 2.4 nHm^2.kg^{-1}. It is comparable with those of previously reported IONP nanoparticles (spherical or cubic ones) permitting the efficient macroscopic magnetothermal heating.[11,12]

To further explore magnetothermal properties of IONP@alkoxyamine nanoparticles, we investigated the influence of the magnetic field strength and solvent nature. First, the experiments were performed at three different amplitudes of AMF (8, 12 and 16 kA.m^{-1}) (Fig. S11, ESI). As expected, the maximal temperature achieved under an application of AMF at 10 min increases with the strength of the magnetic field and no saturation of the heating performance was noted.[12] The calculated SAR values equal to 47, 123 and 205 W.g^{-1} (per g of nanoparticles) for the fields of 8, 12 and 16 kA.m^{-1}, respectively, follow this tendency. Note that the calculated average ILP value is still equal to 2.4 nHm^2.kg^{-1}, as expected.

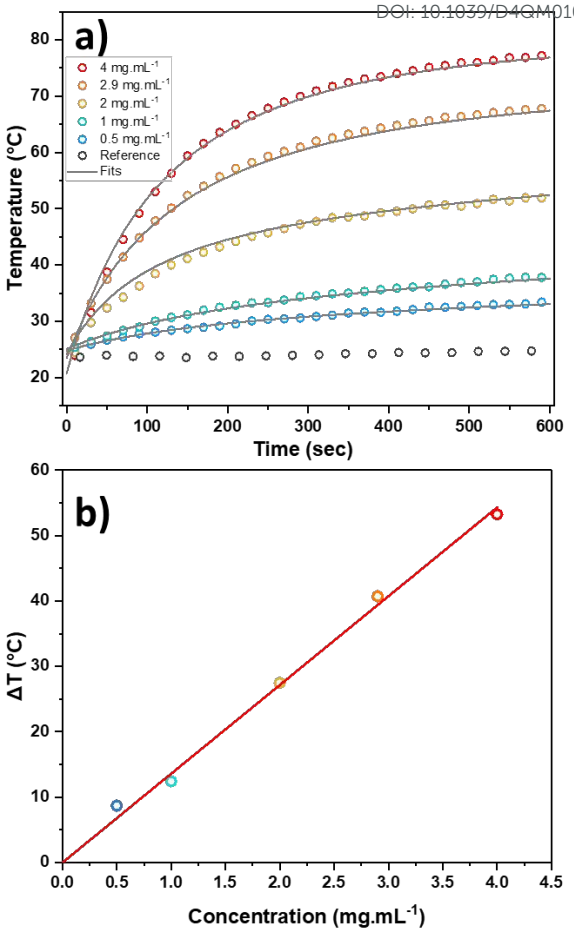

Figure 3. a) Temperature dependence as a function of time for different concentrations of IONP@alkoxyamine nanoparticles colloidal solutions in *tert*-butylbenzene (ranging from 0.1 to 4 mg.mL^{-1}) performed under an ac magnetic field of 20 mT/340 kHz (16 kA.m^{-1}). The grey lines represent the best fits with the second-order Taylor series model. Black empty points indicate the magnetothermal experiments for *tert*-butylbenzene alone used as reference, b) ΔT as a function of the IONP@alkoxyamine nanoparticles concentration.

Secondly, the solvent's properties, particularly their boiling point, viscosity, and specific heat are important parameters in determining the efficiency of magnetothermal heating. Note that, to the best of our knowledge, the influence of solvents on the macroscopic magnetothermal properties was emphasized rather scarcely in the literature.[57] We have primarily assessed the colloidal stability and good dispersibility of our nanoparticles in five selected solvents with varying boiling points and viscosities (octanol, butanol, tert-butylbenzene, propanol, and THF), since these factors are crucial for the magnetothermal performance of the nanoparticles.[58,59] DLS analyses (Fig. S12 (ESI)) demonstrates that the obtained nanoparticles are rather well dispersed. Then, the magnetothermal heating of five different colloidal solutions of IONP@alkoxyamine (2.9 mg.mL^{-1}) in octanol, butanol, *tert*-butylbenzene, propanol and THF were tested with the same AMF strength. Fig. 4 shows that for the same concentration of the nanoparticles, the choice of solvent importantly impacts the

View Article Online
DOI: 10.1039/D4QM01024

macroscopic temperature rise. Fig. 4b-d demonstrates the variation of ΔT as a function of solvent's boiling temperature, dynamic viscosity and specific heat, respectively. As one can see, ΔT increases with the solvent's boiling temperature (Fig. 4b). Note that the measured macroscopic temperature remained below the boiling temperature of the solvents in all cases, even for THF. Indeed, higher boiling point solvents tend to result in greater temperature increases, as they can sustain higher temperatures without undergoing phase changes, thereby reducing heat dissipation and supporting a higher ΔT. This effect was previously reported by B. Chaudret and coll. in their study of the magnetothermal effect on the catalytic activity of iron carbide nanoparticles.[57] They also highlighted the significant discrepancy between the temperature at the nanoparticle surface and the macroscopic temperature measured in the solution, occurring particularly for solvents with relatively low boiling points. A similar trend is observed with the viscosity of the solvent taken at the maximum temperature reached by the colloidal solution (Fig. 4c). Specifically, ΔT increases as the viscosity of the solvent increases. This observation rather contrasts with previously published results for magnetic nanoparticles in water and aqueous agar-agar solutions, where magnetothermal heating either decreased or remained unchanged as viscosity of solution increased.[14,60–62] However, the impact of viscosity on magnetothermal heating is rather complex and can vary depending on several factors, including the Brownian relaxation of magnetic nanoparticles, thermal conductivity, the specific heat of the solvent, etc. The overall effect of viscosity on magnetothermal heating results from the interplay of these factors. In our case, with different solvents being used, higher viscosity may enhance local heating and reduce heat dissipation, leading to a greater observed temperature rise compared to aqueous solutions. Finally, we plotted ΔT as a function of the solvent's specific heat (C_p of solvent is taken at the maximal temperature reached in the experiments), which demonstrated that the macroscopic temperature increase is greater with higher C_p (Fig. 4d). Given that the measurements were performed with the same nanoparticles and under identical conditions, with only the solvents differing, this observation is indeed counterintuitive. However, despite a higher C_p typically requiring more energy to increase the temperature, solvents with a greater C_p can absorb and retain more heat from the nanoparticles. This enhanced heat absorption can result in a more substantial temperature rise in the solvent. Additionally, solvents with higher C_p may experience reduced relative heat loss because they can absorb more heat before a significant temperature increase occurs. This effect can lead to a more pronounced macroscopic temperature increase. Moreover, solvents with higher C_p may facilitate better thermal equilibration within the system, promoting a more even distribution of heat and contributing to a higher overall ΔT. Therefore, the observed impact of solvent properties (boiling point, viscosity, and specific heat) on magnetothermal heating reveals that macroscopic temperature rise during the AMF action requires careful consideration of macroscopic environment.

View Article Online
DOI: 10.1039/D4QM01022A

ARTICLE

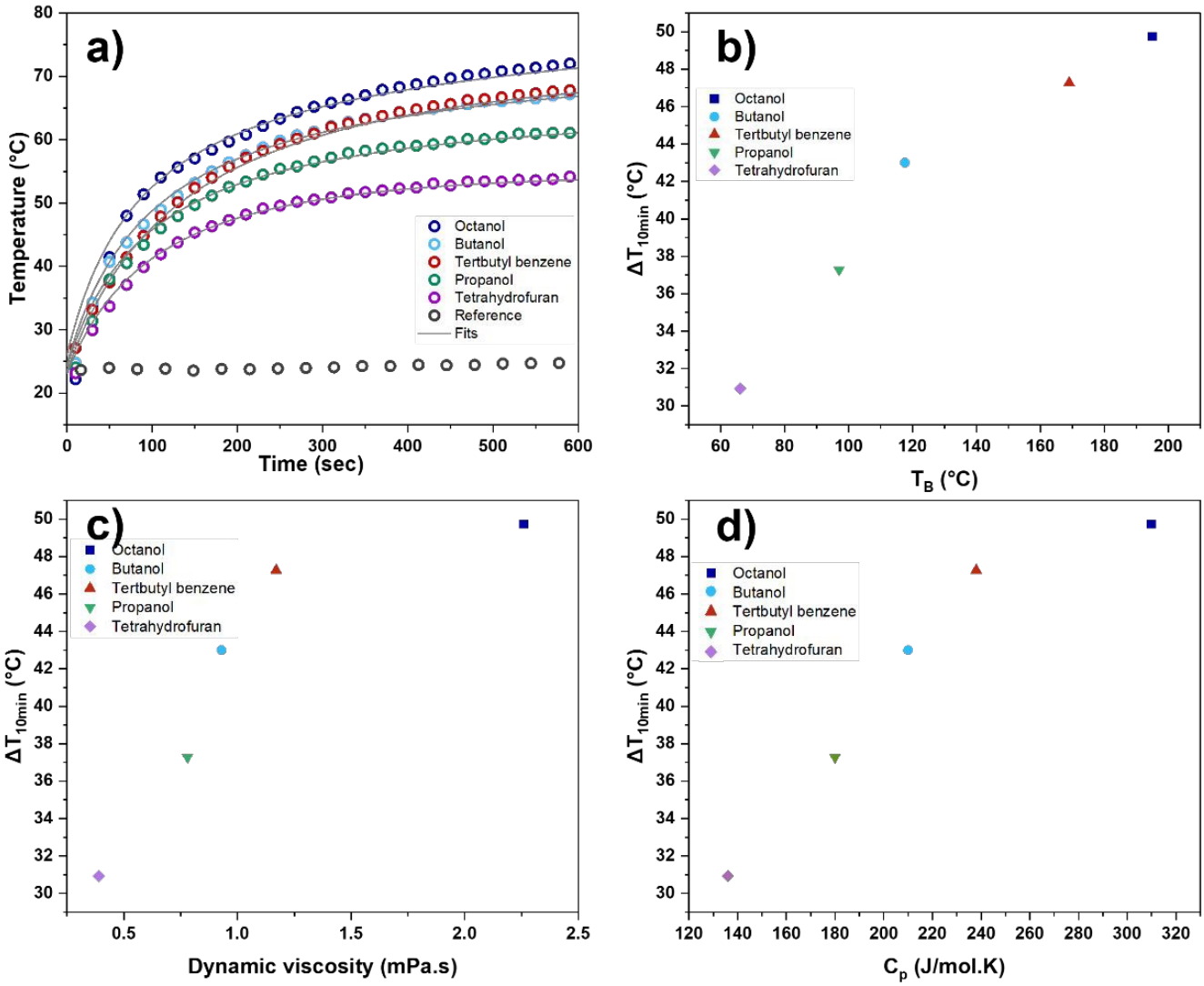

Figure 4. a) Magnetothermal experiments performed for IONP@alkoxyamine colloidal solutions with the concentration of 2.9 mg mL^{-1} in different solvents under applied ac magnetic field of 20 mT/340 kHz. The solid lines represent the best fit with the second-order Taylor series model, b) ΔT as a function of boiling temperature of solvent, c) ΔT as a function of the solvent viscosity, and d) ΔT as a function of the solvent's specific heat (C_p).

View Article Online
DOI: 10.1039/D4QM01022A

ARTICLE

Photothermal properties. Note that investigations into the photothermal properties of IONPs have emerged relatively recently, revealing their ability to efficiently convert near-infrared (NIR) light into heat.[17] Although the precise mechanisms behind this heat generation are not yet fully elucidated, it is known to involve electronic transitions between the valence and conduction bands, with heat produced as electrons return to their original states.[63] Some iron oxide nanoparticles have demonstrated heating capabilities comparable to those of gold nanoparticles, which are considered standard photothermal agents. Moreover, recent studies have shown that certain IONPs can achieve effective photothermal heating at lower concentrations than those typically required for magnetothermia. However, this approach often relies on laser power densities exceeding 1 W/cm². [64]

The photothermal properties of the IONP@alkoxyamine nanoparticles were investigated under a laser irradiation at 808 nm (power 2.6 W.cm^{-2}). The macroscopic temperature of the colloidal solutions with the concentrations 0.1 – 4 mg.mL^{-1} under light irradiation was monitored by using an optical fibre introduced in solution. A macroscopic heating of *tert*-butylbenzene colloidal solutions was observed after a few minutes of irradiation in the presence of nanoparticles, while the nanoparticles-free *tert*-butylbenzene remains unheated (Fig. 5a). The temperature profiles for investigated concentrations (0.1 – 4 mg.mL^{-1}) were drawn for 10 min of irradiation. Fig. 5b shows a ΔT which first increases quasi linearly at low concentration (below 1 mg.mL^{-1}). Then, at 4 mg mL^{-1} a plateau is reached. This well-known effect in the literature can be explained by the limitation of the penetration depth of the laser in the sample due to the optical saturation, limited interaction sites, self-screening and quenching effects.[65,66] Note that, in contrast, magnetothermal heating (Figure 3) is not limited by optical penetration depth, resulting in a more pronounced difference in temperature increase as a function of concentration in the AMF experiments (ΔT until 50 °C at 4 mg.mL). In ESI, a model was developed to describe the shape of the ΔT as a function of the concentration curve. Eq. (19), (see Models and theory part in ESI) describes the evolution of ΔT, which depends exponentially on the thickness of the sample and the concentration of the substance in question. The light-to-heat conversion efficiency (η), which is the conventional parameter employed for the comparison of different photothermal agents, was calculated by fitting the *T vs* time curves at low concentrations with the COMSOL program (see Experimental part for details and Fig. 5). The obtained η value of 30 ± 1 % is among the highest previously reported values for different IONPs.[18]

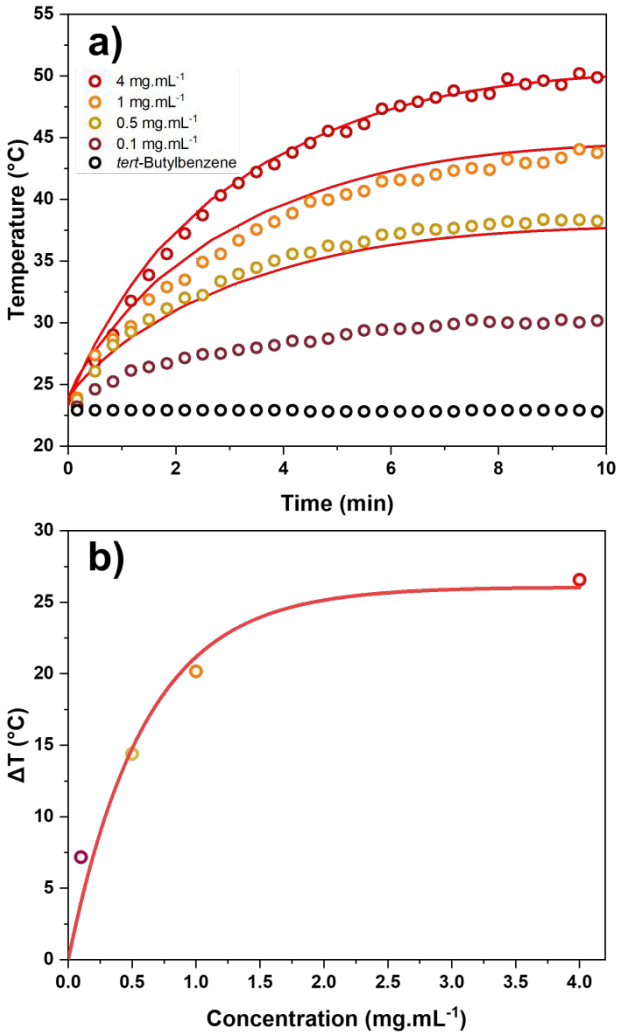

Figure 5. a) Temperature profile *vs* time for IONP@alkoxyamine colloidal solutions with concentrations ranging from 0.1 to 4 mg.mL^{-1} in *tert*-butylbenzene performed under a laser irradiation at 808 nm (laser power of 2.6 W.cm^{-2}). Solid line represents the fit of the curves with the COMSOL program, b) Corresponding ΔT *vs* IONP@alkoxyamine nanoparticles concentration dependence. The red curve represents the fit done using eq. (S19).

Kinetics of radical release

The controlled radical release in a multistep way was investigated by using EPR spectroscopy for: (*i*) free alkoxyamine molecule upon thermal heating in order to determine its activation energy (E_a) and its half-life time, (*ii*) IONP@alkoxyamine nanoparticles under applied AMF, and (*iii*) IONP@alkoxyamine nanoparticles under laser irradiation at 808 nm.

View Article Online
DOI: 10.1039/D4QM01028A

First, the homolysis reaction of *tert*-butylbenzene solution of the free diethyl(6-(4-(1-((di-tert-butylamino)oxy)ethyl) benzamido)hexyl)phosphonic acid (10^{-4} M) was investigated at three different temperatures, 44, 65 and 77 °C, by using the EPR spectroscopy (by taking aliquots and analysing them by EPR) (Fig. 6a). Note that the EPR spectrum of this molecule is silent before thermal activation, while upon heating it shows a three line profile corresponding to the nitroxide (I_N = 1, S = 1/2) generated by the homolysis of the thermosensitive C-ON bond (Fig. 6b).[62] The hyperfine coupling constant is equal to 15.6 G, which is in agreement with previously reported results on nitroxide. This clearly indicates that the free alkoxyamine is stable at room temperature and delivers radicals only upon heating. The kinetic of the radical delivery for three investigated temperatures represented as C/C_0 *vs.* heating time curve (up to 2.5 h) (Fig. 6c) was fitted with the (eq. 1):

$$[rad] = [rad]_\infty(1 - e^{-k_d t}) \quad (1),$$

which is the analytical solution of the following kinetic differential equations:

$$\frac{\mathrm{d}[alkox]}{\mathrm{d}t} = -k_d[alkox] \quad (2) \text{ and}$$

$$\frac{\mathrm{d}[rad]}{\mathrm{d}t} = k_d[alkox] \quad (3),$$

where k_d is the rate homolysis constant, t is the time, [rad] is the concentration of the generated nitroxide during homolysis and $[rad]_\infty$ stands for the concentration of nitroxide when the plateau is reached, *i.e.*, $[rad]_\infty = [alkox]_0$ = 0.1 mM. Then, the Arrhenius law, as set forth in eq. (4), permits to provide the activation energy of the alkoxyamine's homolysis, E_a, and its half-life time, $t_{1/2}$:

$$E_a = -RTln\left(\frac{k_d}{A}\right) \quad (4)$$

The half-life time, $t_{1/2}$, has been determined as $t_{1/2}=(ln2)/k_d$. The employment of these equations allowed to obtain the following parameters (for both temperatures): $k_d = 6.4 \cdot 10^{-4}$ s^{-1} at 77 °C (100 % conversion), E_a = 117.8 kJ.mol^{-1} and $t_{1/2}$ = 33 days at 20 °C. The average pre-exponential factor $A = 2.4 \cdot 10^{14}$ s^{-1} has been fixed for this fit as previously reported.[67] Note that the obtained activation energy is significantly lower (and at lower temperature) in comparison with the previously published by us (6-{4-[1-(2,2,6,6-tetramethyl-piperidin-1-yloxy)-ethyl]-benzoylamino}-hexyl)-phosphonic acid alkoxyamine used for similar purpose, for which we found following parameters $k_d = 7.0 \cdot 10^{-4}$ s^{-1} at 115 °C (91 % conversion), E_a = 130.3 kJ.mol^{-1} and $t_{1/2}$ = 15.6 years at 20 °C.[48] This signifies that the homolysis of our new alkoxyamine can be produced at lower temperature compared to the previously investigated (6-{4-[1-(2,2,6,6-tetramethyl-piperidin-1-yloxy)-ethyl]-benzoylamino}-hexyl)-phosphonic acid or at the same temperature, but much more rapidly. As an example, $t_{1/2}$ is equal to 18 min, 1h18min and 20h

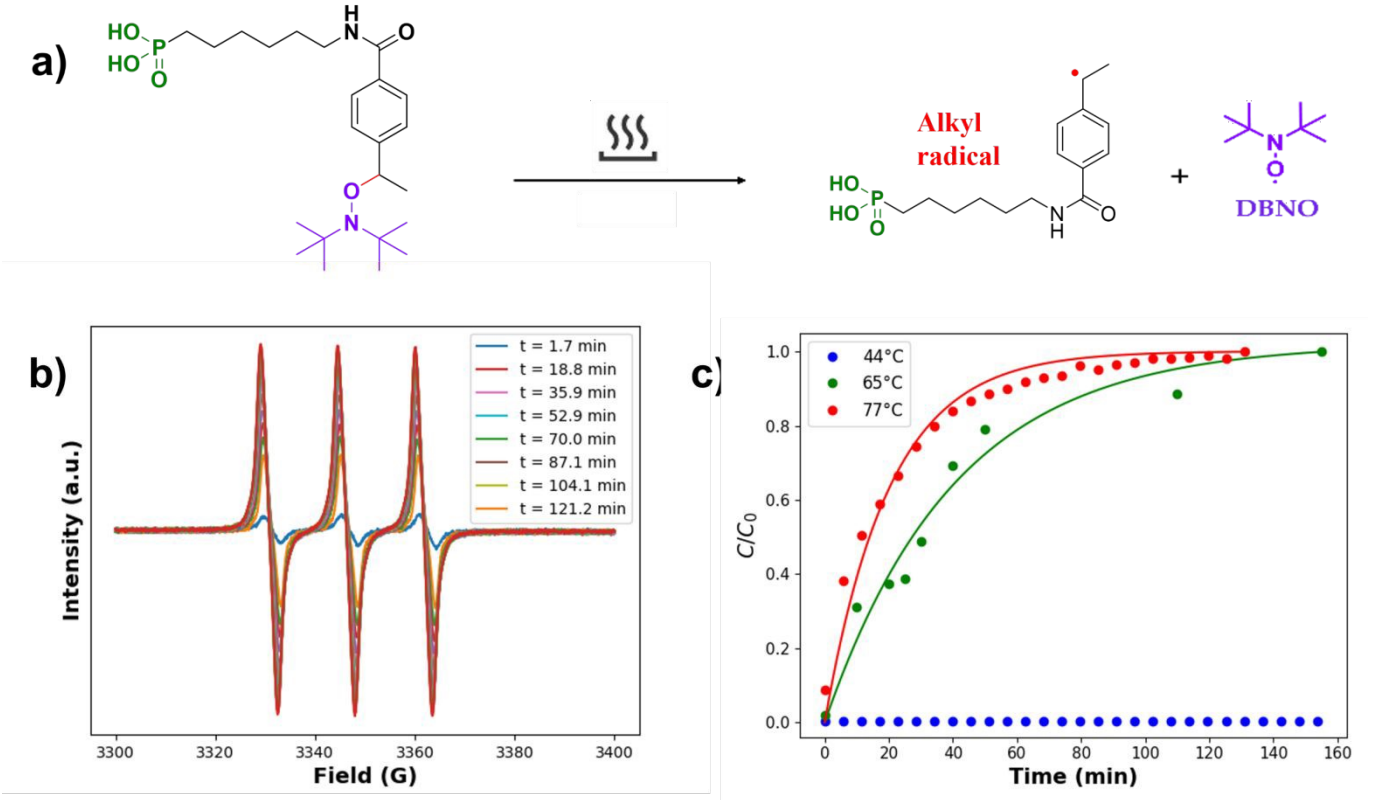

Figure 6. a) Schematic representation of the diethyl(6-(4-(1-((di-tert-butylamino)oxy)ethyl)benzamido)hexyl)phosphonate alkoxyamine homolysis upon heating; b) Representative EPR spectra performed for the diethyl(6-(4-(1-((di-tert-butylamino)oxy)ethyl)benzamido)hexyl)phosphonic acid alkoxyamine before and afer heating at 77 °C during different periods of time; c) C/C_0 *vs.* time curve obtained for alkoxyamine under three different heatings at 44, 65 °C, at 77 °C. Solid line represents the best fit of the curve with eq. (1).

at 77, 65 and 44 °C, respectively.

Second, the radical formation for IONP@alkoxyamine nanoparticles was investigated in *tert*-butylbenzene colloidal solution of 2.9 mg.mL^{-1} upon exposure under an action of AMF of 340 kHz and 20 mT (Fig. 7a). The choice of *tert*-butylbenzene as solvent has been motivated by its high boiling point (169 °C), optimal magnetothermal heating (Fig. 4) and colloidal stability of nanoparticles (Fig. S12, ESI). Fig. 7b shows the macroscopic temperature elevation during the magnetothermal heating of this colloidal solution during 60 min. The temperature rises quickly during the first 12 min, then more gradually and stabilizes at 77 °C for the remainder of the period. To quantify the quantity of radicals formed over time, aliquots were taken from the colloidal solution at precise time intervals. To analyse the presence of radicals by EPR, the magnetic nanoparticles were removed from the samples using a 5T magnet. The EPR spectra of the samples taken before the application of the magnetic field and the ones at 3, 6 and 20 minutes after magnetothermal heating are shown in Fig. 7c. As expected, the EPR spectrum is silent before the application of the magnetic field, indicating that the IONP@alkoxyamine nanoparticles are stable at room temperature, with no radicals formed in the absence of an external *stimulus*. Following the application of AMF, the spectra display three characteristic lines (hyperfine coupling constants of 15.6 G) with increasing intensities over time, indicating a growing quantity of released radicals. The homolysis kinetic is represented here as the time dependence of the normalized concentration, C/C_0, shown on Fig. 7d. The concentration of radicals increases very rapidly during the first 20 min due to efficient C-ON bond homolysis induced by localized heating on the nanoparticle surface triggered by the action of the AMF. At this time, the macroscopic temperature of the colloidal solution reaches 77 °C, with the homolysis rate (alkoxyamine conversion rate) determined to be 94 %. After this, the curve begins to decrease due to the recombination and degradation of the formed radicals. This result successfully demonstrated that the IONP@alkoxyamine nanoparticles generate radicals efficiently under magnetothermal heating. In comparison with the previously published studies on IONP nanoparticles grafted with (6-{4-[1-(2,2,6,6-tetramethyl-piperidin-1-yloxy)-ethyl]-benzoylamino}-hexyl)-phosphonate alkoxyamine, which delivered 70 % of radicals after 100 minutes of exposure to AMF,[48] the current system exhibits nearly complete homolysis (94 %) after just 20 min of exposure demonstrating therefore superior performance.

Since the thermosensitive alkoxyamines are directly attached to the surface of the nanoparticles, their homolysis reaction can be used to estimate the surface temperature of the nanoparticles. Fig. 7d demonstrates a bell-shaped curve for the C/C_0 *vs.* time dependence. As previously stated, this behaviour can be attributed to a recombination of the radical. For this purpose, the previous model described by eq. (2) and (3) is replaced by the following theoretical model to fit the C/C_0 *vs time* curve. The evolution of the radical's concentration over time can be expressed using the coupled eqs. (5) and (6):

$$\frac{\mathrm{d}[alkox]}{\mathrm{d}t} = -k_d[alkox] \quad (5)$$

$$\frac{\mathrm{d}[rad]}{\mathrm{d}t} = k_d[alkox] - k_1[rad] \quad (6).$$

The initial equation serves to model the kinetic chemical reaction, whereby radicals are produced from alkoxyamine grafted to the surface of IONP, governed by the homolysis rate constant, k_d. The second equation describes the temporal evolution of the concentration of radicals produced and recombined, where k_1 is the recombination constant. Note that we assumed the recombination of radicals follows a pseudo-first-order reaction for simplicity. The k_d constant follows the Arrhenius law:

$$k_d = A \times \exp(-E_a/RT(t)) \quad (7),$$

where the values of the pre-exponential factor *A* and the energy barrier E_a were fixed for the free alkoxyamine molecule's homolysis. In this equation, *T(t)* term represents the variation of the temperature on the surface of the nanoparticles as a function of time. For simplicity, it was assumed that the temperature at the nanoparticle surface follows the Newton's law of cooling. It can be expressed by eq. (8):

$$T(t) = (T_{max} - T_0)(1 - \exp(-t/\tau_T)) + T_0 \quad (8)$$

where T_0 is the initial temperature (room temperature), T_{max} is the maximal temperature and τ_T is the heating rate. Theoretical curves were obtained through the numerical solution of eq. (5) and (6), in conjunction with the utilisation of eq. (7) and (8).

The best fit of the experimental C/C_0 *vs time* curve with this equation afforded the following parameters: T_{max} = 86 ± 1 °C, k_1 = (4.2 ± 0.3)·10^{-5} s^{-1}, τ_T = 59 ± 13 s. This result indicates that the maximum temperature for complete homolysis, as determined by fitting, is higher than the macroscopic temperature measured by the optical fibre or thermal camera. Variations of the homolysis rate constant as a function of temperature and time are provided in Fig. S13a, b (ESI). Therefore, by using eq. (8), we were able to plot the homolysis temperature as a function of time. This temperature corresponds to the region close to the nanoparticles' surface (approximately 15–20 Å from the surface). Fig. 7e compares the macroscopic temperature of the colloidal solution with the estimated homolysis temperature, highlighting a substantial discrepancy. The homolysis temperature rises rapidly to 86 °C within 2.5 minutes and then stabilizes, whereas the macroscopic temperature only reaches 77 °C after 12 minutes. This discrepancy could be explained by two hypotheses:

(*i*) The presence of a localised heating within the thin corona, just in a few nanometers around the nanoparticles, could result in a temperature significantly higher than that in the bulk solution. The rapid rise and stabilization of the homolysis temperature near the nanoparticles suggest that these nanoscale regions experience more intense thermal conditions than the bulk solution. After 12 minutes, the ΔT between the surface and bulk solution temperatures was measured at 9 °C, in good agreement with our previous experiments.[48] Although

View Article Online
DOI: 10.1039/D4QM01022A

still a topic of debate, the existence of a "hot spot" effect in IONP subjected to AMF has been previously proposed under certain conditions in the literature.[10,68–72]

(*ii*) Alternatively, a catalytic effect under AMF could be accelerating the homolysis reaction specifically at the surface of the alkoxyamine-grafted nanoparticles, enhancing the reaction rate locally and independently of the overall solution temperature. Some catalytic effects under magnetic field application, including AMF, have indeed been reported in the literature.[73] Note also that compared to the free alkoxyamine (6-(4-(1-((di-tert-butylamino)oxy)ethyl) benzamido)hexyl)phosphonic acid heated at 77 °C, AMF exposure accelerates the homolysis of alkoxyamine-grafted nanoparticles (16 kA·m^{-1}, 2.9 mgmL^{-1}) twofold ($t_{1/2}$ = 7.9 min for IONP@alkoxyamine *vs* 18 min for alkoxyamine). Moreover, almost 1h required for $t_{1/2}$ conversion in our earlier IONP grafted with (6-{4-[1-(2,2,6,6-tetramethyl-piperidin-1-yloxy)-ethyl]benzoylamino}-hexyl)-phosphonate alkoxyamine nanoparticles at higher temperature (110 °C).[48]

Third, the radical formation was also investigated under laser irradiation (photothermal heating). For this, the colloidal solution of the IONP@alkoxyamine nanoparticles of the optimal concentration of 1 mg.mL^{-1} was continually irradiated at 808 nm at the power of 2.6 W.cm^{-2} during 10, 20 and 60 min. For each time, the magnetic nanoparticles were separated by magnetic decantation, and the remaining supernatants were analysed by EPR to quantify the radical release. The EPR spectrum is silent before irradiation, indicating that no radicals were present in the initial solution. However, after 10 minutes of irradiation, three characteristic lines appear in the EPR spectrum, signalling

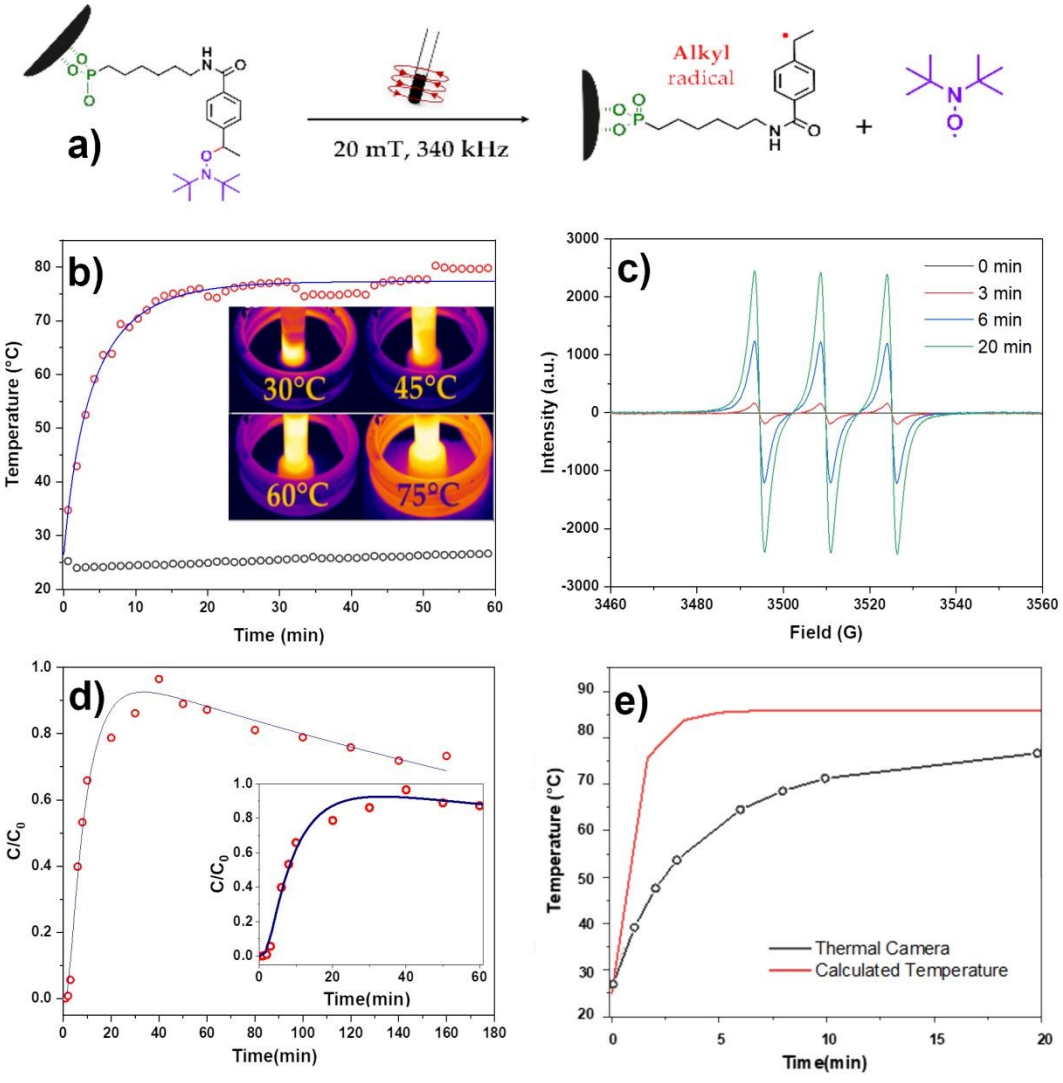

Figure 7. a) Schematic representation of the alkoxyamine homolysis in IONP@alkoxyamine nanoparticles under AMF; b) Temperature as a function of time curve for IONP@alkoxyamine nanoparticles (2.9 mg.mL^{-1}) exposed to AMF (340 kHz and 20 mT) (red circles) and *tert*-butylbenzene without nanoparticle taken as reference (grey circles). Solid line represents the best fit of the curve with the second-order Taylor series model. Inset: Thermal images recorded by thermal camera during this experiment, c) EPR spectra for the colloidal solution of IONP@alkoxyamine (2.9 mg.mL^{-1}) at different time of exposure to AMF (340 kHz and 20 mT); d) Homolysis kinetics represented as the C/C_0 *vs. time* curve for IONP@alkoxyamine (2.9 mg.mL^{-1}) at different time of AMF exposure (340 kHz and 20 mT). Solid line represents the best fit with the couple of eq. (5) and (6). Inset: Magnification of the curve in the 0 – 60 min intervale of time; e) Evaluation of measured macroscopic temperature (black curve) and determine homolysis temperature (red curve) as a function of time during magnetothermal heating of IONP@alkoxyamine nanoparticles.

View Article Online
DOI: 10.1039/D4QM01083A

the presence of radicals (Fig. 8a). The intensity of these lines increases with continued irradiation. The nitrogen hyperfine coupling constant is equal to 15.6 G. The C/C_0 *vs*. time curve for photothermal activation of homolysis shown in Fig. 8b reveals that a half conversion ($t_{1/2}$) is achieved after 23.6 min at 44 °C, while the free molecule requires 20 h to reach the same conversion at this temperature. This finding demonstrates that radical production can be achieved through photothermal activation at temperatures not exceeding 44 °C (see Fig. 5a for temperature measurements during photothermal heating). Note also that the continuous irradiation of the free alkoxyamine molecule in the same conditions (808 nm, 2.6 W.cm^{-2}, *tert*-butylbenzene) did not give the appearance of clear radical's signal in the EPR spectrum (Fig. S14, ESI). A similar experiment was performed at the same nanoparticles' concentration of 2.9 mg·mL^{-1} as used in the magnetothermal studies, allowing for a comparison between magnetothermal and photothermal effects (Fig. S15, ESI). In this case, a half-conversion time of $t_{1/2}$ = 12.7 min was observed.

Eqs. (2) and (3), as well as the macroscopic temperature (T) monitored during the experiments were used to fit the C/C_0 *vs time* curves to obtain the real homolysis temperature in the vicinity of the nanoparticles surface (T+ΔT) (solid line on Fig. 8b and Fig. S15, ESI). For the nanoparticles concentration of 1 mg.mL^{-1}, the following parameters were obtained: T_{max} = 107 ± 5 °C, k_d = 1.5·10^{-2}s^{-1}. Notably, a very significant discrepancy (ΔT) of 63 °C was observed between the measured macroscopic temperature of the solution (44 °C) and the temperature near the nanoparticle surfaces (107 °C). Comparable results were obtained for the photothermal experiment performed at a concentration of 2.9 mg·mL^{-1}, with a discrepancy ΔT = 59 °C between macroscopic and local temperatures. This pronounced difference suggests that the alkoxyamine homolysis occurring at the nanoparticle surface under light irradiation is considerably more intense than what would be expected based on the bulk solution heating alone. This phenomenon also observed under AMF, though it appears even more pronounced in the case of photothermal activation. To explain this discrepancy, two hypotheses should also be considered. Firstly, the intense local heating observed in photothermal experiments could result from a localized photothermal effect, leading to more concentrated heating than magnetothermal activation due to distinct mechanisms of heat generation and dissipation. Secondly, an autocatalytic homolysis effect under light irradiation may also be influencing the process, particularly for alkoxyamines grafted onto the nanoparticle surface. For instance, thermosensitive alkoxyamine derivatives covalently attached to spherical Au nanoparticles via pendant -NH_2 groups have shown the capacity to generate radicals through plasmonic activation by light irradiation without heating of the bulk solution.[74] Notably, in the absence of IONPs, the alkoxyamine alone did not produce radicals under identical irradiation conditions.

These results highlight the critical importance of localized nanoscale effects, demonstrating that the alkoxyamine's homolysis rate at the nanoparticle surface submitted to the action of external *stimuli* is significantly elevated compared to consideration of only a bulk solution heating. This enhancement is even much more pronounced under light irradiation. Further investigation is required to determine the primary factors driving alkoxyamine homolysis in this context.

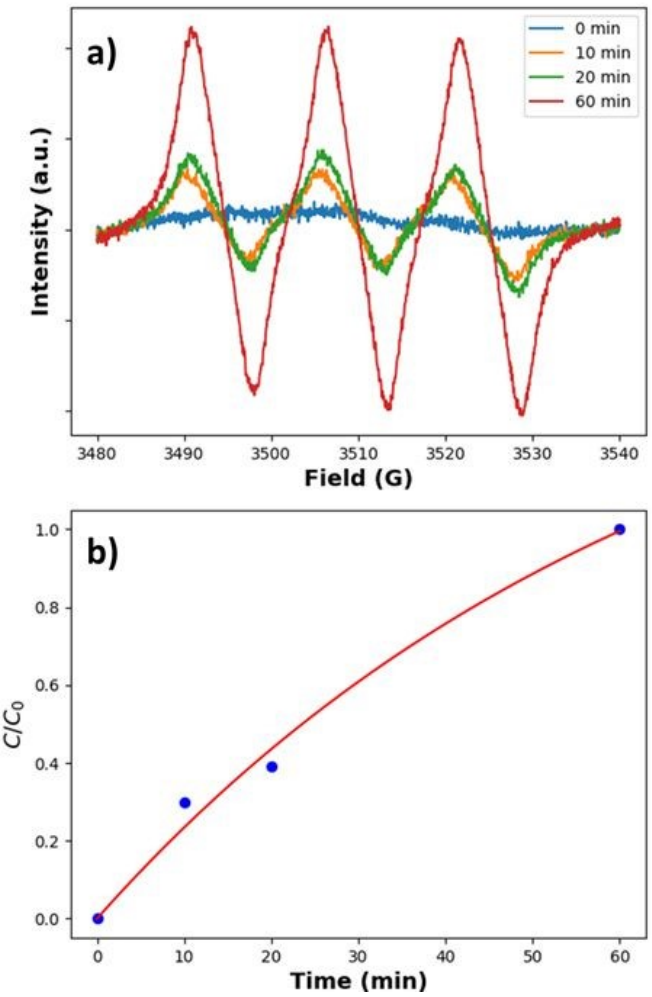

Figure 8. (a) EPR spectra for the *tert*-butylbenzene solutions of IONP@alkoxyamine (1 mg.mL^{-1}) before and after 10, 20 and 40 min after light irradiation at 808 nm (2.6 W.cm^{-2}); (b) Homolysis kinetic represented as C/C_0 *vs* time curve. The red line represents the best fit with the Eq. (2) and (3).

Experimental part

Materials

All chemical reagents were purchased from commercial suppliers (Sigma-Aldrich, Sikémia, and TCI) and used without further purification. Ferric hydroxide oxide (FeO(OH) hydrated, 30-50 mesh), oleic acid (90%) and oleylamine (90%) from Sigma Aldrich; n-docosane (99%) from Acros organic. Pentane, diethyl ether, cyclohexane, acetone and ethanol were purchased from Merck. All organic chemistry experiments were performed under anhydrous conditions and an inert atmosphere of argon and, except where stated, using dried apparatus, and employing standard techniques for handling air-sensitive materials. Routine reaction monitoring was performed using silica gel 60 F254 TLC plates; the spots were visualized upon exposure to UV

View Article Online
DOI: 10.1039/D4QM01022A

light and a *p*-anisaldehyde or phosphomolybdique acid solution in EtOH followed by heating. Purifications were performed on chromatography columns with silica gel grade 60 (230–400 mesh).

Syntheses

Syntheses of the DBNO alkoxyamine derivative.

Methyl 4-vinylbenzoate: A solution of 4-vinylbenzoic acid (5.00 g, 33.8 mmol, 1 eq.) and K_2CO_3 (45.8 g, 331 mmol, 9.8 eq.) were stirred under argon, at room temperature. Then, iodomethane (2.50 mL, 40.5 mmol, 1.2 eq.) was added slowly. The reaction was controlled by TLC (DCM/MeOH 95:5). After the reaction, water was added to the reaction mixture, and the reaction mixture was extracted with Et_2O. The organic layer was washed with water and dried on $MgSO_4$, and the solvent was removed under a vacuum. The crude was purified by column chromatography (DCM/MeOH gradient from 0% to 5% of MeOH) to yield methyl-4-vinylbenzoate quantitatively. The ^1H spectra of this compound were identical to the one reported.[11] ^1H NMR (300 MHz, $CDCl_3$): δ 8.10–7.89 (m, 2H, $H_{(2,4)}$), 7.52–7.39 (m, 2H, $H_{(1,5)}$), 6.75 (dd, J = 17.6, 10.9 Hz, 1H, $H_{(7)}$), 5.86 (dd, J = 17.6, 0.5 Hz, 1H, $H_{(8Z)}$), 5.38 (d, J = 10.9 Hz, 1H, $H_{(8E)}$), 3.91 (s, 3H, $H_{(10)}$).

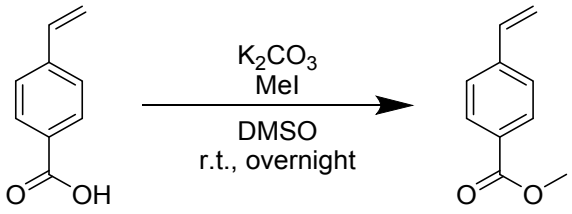

Methyl 4-(1-((di-tert-butylamino)oxy)ethyl)benzoate: In an open-air flask, Methyl 4-(1-((di-tert-butylamino)oxy)ethyl) benzoate and $MnCl_2$ (73 mg, 0.37 mmol, 0.1 eq.) were added to a stirred solution of salen ligand (99 mg, 0.37 mmol, 0.1 eq.) in THF. After 30 minutes of stirring at room temperature, a solution of di-tert-butyl-nitroxide radical (DBNO) (0.81 g, 5.55 mmol, 1.5 eq.) and methyl 4-vinylbenzoate (0.60 g, 3.70 mmol, 1 eq.) in THF was added, then, $NaBH_4$ powder (4 eq.) was added in small portions. The resulting suspension was stirred at room temperature for 24 h. It was then diluted with EtOAc and 1 M aq. HCl was carefully added up to pH~1-2. Solid $NaHCO_3$ was then added until neutralization. The layers were separated, and the organic phase was washed with water, then brine and dried over $MgSO_4$. After concentrating under reduced pressure, the residue was purified by column chromatography (EP/Et_2O gradient from 0% to 6% of Et_2O) to yield methyl 4-(1-((di-tert-butylamino)oxy)ethyl)benzoate (0.83 g, 73%). ^1H NMR (400 MHz, $CDCl_3$): δ 8.01–7.97 (m, 2H, $H_{(2,4)}$), 7.42–7.37 (m, 2H, $H_{(1,5)}$), 4.88 (q, J = 6.7 Hz, 1H, $H_{(7)}$), 3.91 (s, 3H, $H_{(10)}$), 1.49 (d, J = 6.7 Hz, 3H, $H_{(8)}$), 1.32 (s, 3xCH_3, $H_{(14)}$), 1.03 (s, 3xCH_3, $H_{(13)}$). ^{13}C NMR (101 MHz, $CDCl_3$): δ 167.1 (CO, $C_{(9)}$), 150.7 (Cq, $C_{(6)}$), 129.4 (2xCH, $C_{(2,4)}$), 128.6 (Cq, $C_{(3)}$), 126.6 (2xCH, $C_{(1,5)}$), 82,7 (CH, $C_{(7)}$), 62.0 (Cq, $C_{(11)}$), 61.8 (Cq, $C_{(12)}$), 51.9 (CH_3, $C_{(10)}$), 30.7 (3xCH_3, $C_{(13)}$), 30.6 (3xCH_3, $C_{(14)}$), 22.8 (CH_3, $C_{(8)}$). HRMS (ESI): calc. $[M + H]^+$: 308.2220; found: 308.2218.

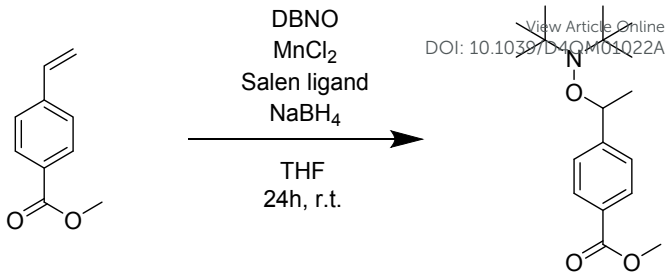

4-(1-((di-tert-butylamino)oxy)ethyl)benzoic acid: KOH (0.84 g, 15 mmol, 8 eq.) was added to a solution of the ester-based alkoxyamine (0.95 g, 2.98 mmol, 1 eq.) in THF-H_2O-MeOH (1 : 1: 1) at room temperature. The mixture was stirred for 6h and, then acidified with 1 M HCl. The mixture was diluted with water and extracted with DCM. The combined organic phase was dried on $MgSO_4$ and the solvent was evaporated. The crude was purified by column chromatography (DCM : MeOH gradient from 0 % to 5 % of MeOH) to afford 4-(1-((di-tert-butylamino)oxy)ethyl)benzoic acid in 92% yield (840 mg). ^1H NMR (300 MHz, $CDCl_3$): δ 9.96 (br s, 1H, COOH), 8.95–7.85 (m, 2H, $H_{(2,4)}$), 7.30–7.22 (m, 2H, $H_{(1,5)}$), 4.74 (br q, J = 5.5 Hz, 1H, $H_{(7)}$), 1.33 (br d, J = 5.4 Hz, 3H, $H_{(8)}$) 1.15 (s, 3xCH_3, $H_{(13)}$), 0.87 (s, 3xCH_3, $H_{(14)}$). ^{13}C NMR (75 MHz, $CDCl_3$): δ 172.1 (CO, $C_{(9)}$), 151.8 (Cq, $C_{(6)}$), 130.3 (2xCH, $C_{(2,4)}$), 128.1 (Cq, $C_{(3)}$), 126.7 (2xCH, $C_{(1,5)}$), 82.9 (CH, $C_{(7)}$), 62.4 (Cq, $C_{(11)}$), 62.1 (Cq, $C_{(12)}$), 30.8 (3xCH_3, $C_{(13)}$), 30.2 (3xCH_3, $C_{(14)}$), 23.7 (CH_3, $C_{(8)}$). HRMS (ESI): calc. $[M + H]^+$: 294.2064; found: 294.2060.

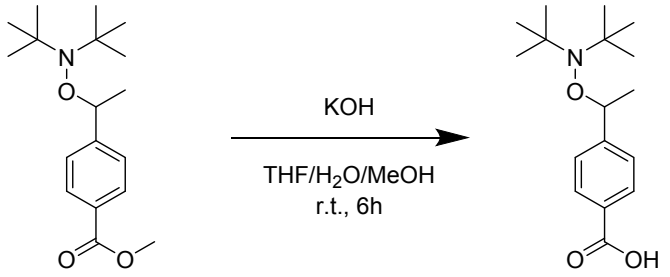

Diethyl(6-(4-(1-((di-tert-butylamino)oxy)ethyl)benzamido) hexyl)phosphonate: DMAP (47 mg, 0.39 mmol, 0.3 eq.) was added to a stirred solution of alkoxyamine (500 mg, 1.63 mmol, 1 eq.) in DCM (5 mL) and the solution was stirred at room temperature under argon for 10 min. After the addition of EDCI (0.38 g, 2.45 mmol, 1.5 eq.), the solution was stirred at room temperature for a further 30 min, then, the amine (503 mg, 2.12 mmol, 1.3 eq.) was added at 0 °C. The reaction mixture was stirred at room temperature overnight. The mixture was washed with HCl 1 M, $NaHCO_3$ (saturated solution), distilled water, and brine. The organic phase was dried with $MgSO_4$, and the solvent was removed under a vacuum. The purification by column chromatography (DCM/MeOH from 0% to 6% of MeOH) yielded diethyl(6-(4-(1-((di-tert-butylamino)oxy)ethyl) benzamido)hexyl)phosphonate (0.835 g, 99%). ^1H NMR (300 MHz, $CDCl_3$): δ 7.71-7.65 (m, 2H, $H_{(2,4)}$), 7.27–7.22 (m, 2H, $H_{(1,5)}$), 6.80 (t, J = 5.5 Hz, 1H, NH), 4.76 (q, J = 6.7 Hz, 1H, $H_{(7)}$), 4.04–3.90 (m, 4H, $H_{(21)}$), 3.32 (dd, J = 12.9, 6.8 Hz, 2H, $H_{(15)}$), 1.38 (d, J = 6.7 Hz, 3H, $H_{(8)}$), 1.21 (t, J = 7.1 Hz, 2xCH_3, $H_{(22)}$), 1.21 (s, 3xCH_3, $H_{(13)}$), 1.70-1.15 (m, 10H, $H_{(16,17,18,19,20)}$), 0.93 (s, 3xCH_3, $H_{(14)}$). ^{13}C

View Article Online
DOI: 10.1039/D4QM01032A

NMR (75 MHz, $CDCl_3$): δ 167.4 (CO, $C_{(9)}$), 148.7 (Cq, $C_{(6)}$), 133.2 (Cq, $C_{(3)}$), 126.8 (2xCH, $C_{(2,4)}$), 126.7 (2xCH, $C_{(1,5)}$), 82.6 (CH, $C_{(7)}$), 61.9 (Cq, $C_{(11)}$), 61.7 (Cq, $C_{(12)}$), 61.3 (d, J_{C-P} = 6.5 Hz, 2xCH_2, $C_{(21)}$), 39.7 (CH_2, $C_{(15)}$), 30.63 (3xCH_3, $C_{(13)}$), 30.58 (3xCH_3, $C_{(14)}$), 30.0 (d, J_{C-P} = 16.3 Hz, CH_2, $C_{(19)}$), 29.3 (CH_2, $C_{(16)}$), 26.3 (CH_2, $C_{(17)}$), 25.4 (d, J_{C-P} = 140.4 Hz, CH_2, $C_{(20)}$), 22.8 (CH_3, $C_{(8)}$), 22.2 (d, J_{C-P} = 5.1 Hz, CH_2, $C_{(18)}$), 16.4 (d, J_{C-P} = 6.0 Hz, 2xCH_3, $C_{(22)}$). ^{31}P NMR (162 MHz, $CDCl_3$): δ 32.26. HRMS (ESI): calc. $[M + H]^+$: 513.3452; found: 513.3452.

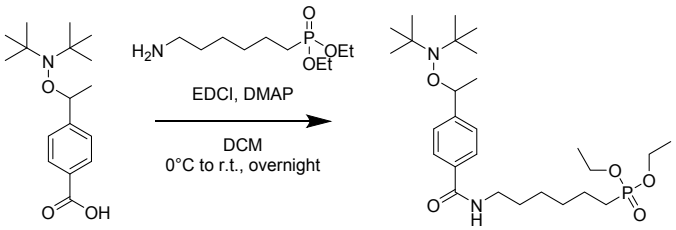

(6-(4-(1-((di-tert-butylamino)oxy)ethyl)benzamido)hexyl) phosphonic acid: The phosphonate-based alkoxyamine (835 mg, 1.63 mmol, 1 equiv.) was dissolved in DCM (25 mL) and cooled at −20 °C. Then, TMSBr (780 µL, 3.5 equiv.) was added and the reaction was stirred 3h at room temperature. The solvent was evaporated under reduced pressure and the residual mixture was dissolved in methanol (20 mL) and stirred for 30 min. The solvent was evaporated under reduced pressure to yield (6-(4-(1-((di-tert-butylamino)oxy)ethyl)benzamido)hexyl)phosphonic acid as a white powder, which was pure enough to be used without further purification. (743 mg, quantitative). ^{1}H NMR (300 MHz, MeOD): δ 7.87–7.83 (m, 2H, $H_{(2,4)}$), 7.58–7.54 (m, 2H, $H_{(1,5)}$), 5.84 (q, J = 6.4 Hz, 1H, $H_{(7)}$), 3.36 (t, J = 7.1 Hz, 2H, $H_{(15)}$), 1.35-1.76 (m, 5xCH_2, $H_{(16,17,18,19,20)}$), 1.72 (d overlapped, J = 6.4 Hz, 3H, $H_{(8)}$), 1.73 (s, 3xCH_3, $H_{(13)}$), 1.40 (s, 9H, $H_{(14)}$); ^{13}C NMR (75 MHz, MeOD): δ 169.3 (CO, $C_{(9)}$), 145.4 (Cq, $C_{(6)}$), 136.0 (Cq, $C_{(3)}$), 128.9 (2×CH, $C_{(2,4)}$), 127.9 (2×CH, $C_{(1,5)}$), 87.9 (CH, $C_{(7)}$), 77,4 (Cq, $C_{(11)}$), 77.0 (Cq, $C_{(12)}$), 40.9 (CH_2, $C_{(15)}$), 31.2 (d, J_{C-P} = 16.5 Hz, CH_2, $C_{(19)}$), 30.2 (CH_2 , $C_{(16)}$), 28.64 (3xCH_3, $C_{(13)}$), 28.62 (3xCH_3, $C_{(14)}$), 27.8 (d, J_{C-P} = 137.1 Hz, CH_2, $C_{(20)}$), 26.9 (CH_2, $C_{(17)}$), 24.4 (CH_3, $C_{(8)}$), 23.70 (d, J_{C-P} = 5.0 Hz, CH_2, $C_{(18)}$); ^{31}P NMR (121 MHz, MeOD): δ 30.11; HRMS (ESI) calc. $[M + H]^+$: 457.2826; found: 457.2827.

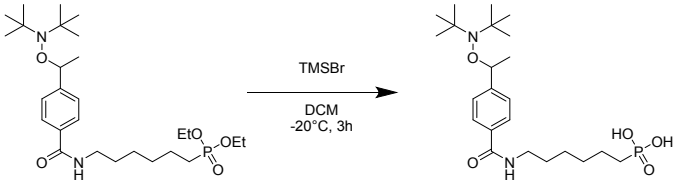

Synthesis of pristine iron oxide nanoparticles IONP@OA/OAm: The pristine IONP of ca. 25 nm stabilized by oleate (OA) and oleyl amine (OAm) were prepared by adapting the previously published procedure involving flash decomposition of FeO(OH) precursor in n-docosane.[75] First, a mixture of FeO(OH) (2.1 mmol, 0.186 g), oleic acid (10 mmol, 3.17 g) and n-docosane (5.02 g) was dried under vacuum for 30 min at room temperature. The mixture was heated to 350 °C under argon flow with a heating rate of 10 °C min^{-1} and the temperature was maintained for a further 90 min under stirring. Then, the temperature was cooled down to 200 °C, the system was open to air and the temperature was maintained at 180 °C for a further 90 min to realize the oxidation of FeO nanoparticles to Fe_3O_4. The temperature was decreased to 50 °C and cyclohexane (15 mL) was added to precipitate the nanoparticles. The obtained solid was washed two times by dispersing in diethyl ether, followed by precipitation with ethanol (1:1 v/v), and then recovered using centrifugation (20,000 rpm, 10 min). Oleylamine (200 µL) was added to the collected material as additional stabilizer. The resultant oleate/oleylamine-capped IONP/OA/OAm nanoparticles were finally dispersed in THF (15 mL) for storage.[48]

Synthesis of IONP@alkoxyamine: The grafting of the alkoxyamine derivative (6-(4-(1-((di-tert-butylamino)oxy)ethyl)benzamido)hexyl) phosphonic acid on the surface of IONP/OA/OAm was performed by a ligand exchange method thanks to the pending phosphonate groups of alkoxyamine.[48] For this, 200 mg of (6-(4-(1-((di-tert-butylamino)oxy)ethyl)benzamido)hexyl) phosphonic acid was dissolved in 20 mL of THF/MeOH (95/5 (vol. %)), and mixed with a suspension of 1 $mg.ml^{-1}$ of IONP/OA/OAm in 20 mL THF. The mixture was then sonicated for 10 min. and rotary stirred at 300 rpm at room temperature for 48 hours. The as-obtained IONP@alkoxyamine nanoparticles were then collected by magnetic separation and washed three times with MeOH. The nanoparticles were then stored in MeOH or dried for further characterizations.

Characterizations

Transmission Electronic Microscopy (TEM) measurements were performed by using LaB6 JEOL 1400 Flash electronic microscope at 100 kV. Dynamic light scattering (DLS) measurements were performed on a Zetasizer Nano-series Malvern instrument (ZEN3600) in order to determine the hydrodynamic diameter of the nanoparticles. Powder X-Ray diffraction (PXRD) was performed using a PANalytical X'Pert Powder analytical diffractometer mounted in a Debye−Scherrer configuration and equipped with Cu radiation (λ = 1.5418 Å). Infrared spectra using attenuated total reflectance (ATR-IR) were recorded using PerkinElmer Spectrum Two FT-IR Spectrometer. Quantifications of P and Fe elements were performed using a Scanning electron microscope equipped with an Energy Dispersive X-Ray analyser (SEM-EDX) on a FEI Quanta FEG 200 instrument. The powders were deposited on an adhesive carbon film and analysed under vacuum. ^{1}H nuclear magnetic resonance (NMR) spectra were recorded using an internal deuterium lock at ambient temperatures on the following instruments: Bruker AC400 (400 MHz). Data were presented as follows: chemical shift (in ppm), integration, multiplicity (s = singlet, d = doublet, t = triplet, m = multiplet, br means the signal is broad, dd = doublet of doublets), coupling constant (*J* in Hz) and integration. ^{13}C nuclear magnetic resonance (NMR) spectra were recorded using an internal deuterium lock at ambient temperatures on the following instruments: Bruker AC400 (101 MHz). ^{31}P nuclear magnetic resonance (NMR) spectra were recorded on a Bruker AC400 (162 MHz) spectrometer with complete proton

decoupling. High-resolution mass spectra (HRMS) were performed on a SYNAPT G2 HDMS (Waters) spectrometer equipped with atmospheric pressure ionization source (API) pneumatically assisted. Samples were ionized by positive electrospray mode as follows: electrospray tension (ISV): 2800 V; opening tension (OR): 20 V; nebulization gas pressure (nitrogen): 800 L/h. Low resolution mass spectra were recorded on ion trap AB SCIEX 3200 QTRAP equipped with an electrospray source. The parent ion (M^+, $[M+H]^+$, $[M+Na]^+$ or $[M+NH_4]^+$) is quoted.

Magnetothermia measurements

Magnetothermia experiences were realized using an ac magnetic field generator (UltraFlex) at 340 kHz. The generating magnetic field is around 20 mT (16 $kA.m^{-1}$). The samples were measured in liquid state. A thermal camera OPTRIS PI 450i and/or optic fibre were used to record the temperature elevation. They provide very similar results.

Photothermal measurements

The photothermal efficiency was measured by placing 300 µL of a colloidal solution in a quartz tube placed in a quartz cuvette. The cuvette was then placed in line with the laser, which irradiated at 808 nm with a power of 2.6 $W.cm^{-2}$. An optic fibre enabling the temperature reading each 30 seconds was placed in the solution. The ΔT were extracted after 10 minutes of exposure to the external *stimuli* (magnetic field or laser irradiation).

EPR investigations of the radical's formation

EPR was performed using the Elexsys E500 CW spectrometer from Bruker, in X band (around 9.8 GHz), dressed with a resonant cavity ER4122SHQ. Samples were analysed using 50 µL capillary tubes (from Hirschmann), sealed with silicon paste. Samples were carefully placed at the same positions. Analyses were made at room temperature, with a window of 10 mT (100G) centred around g=2, an amplitude of 1 G, a frequency of 100 kHz, and a microwave power of 10 db.

Radical release simulations

The radical release simulations were conducted by employing the solution of equations (5) and (6), in conjunction with equations (7) and (8). A custom-built Python routine was created to solve these equations numerically, utilising the "*solve_ivp"* function from the "*scipy.integrate"* package. The optimisation of the fit parameters was achieved through the use of the "*curve_fit"* function from the "*scipy.optimize*" library.

Photothermal modelling

The photothermal modelling was conducted using the COMSOL software,[76] which was employed for the purpose of solving the heat equation. The COMSOL software facilitated the incorporation of shape and volume aspects pertaining to the experimental sample. The sample was not regarded as isolated, and the thermal flux was optimized at its surfaces to facilitate the modelling of the temperature plateau. The light-to-heat conversion coefficient was employed as a fitting parameter within the power source term of the heat equation. Furthermore, the light absorption at 808 nm of the sample was also optimised in order to enhance the precision of the fit result. Three experimental curves were optimized simultaneously in order to obtain an accurate value for the light-to-heat conversion parameter.

Conclusions

In summary, this article reports on a novel nano-system capable of providing localized radical release, remotely triggered by two external *stimuli*, AMF or laser irradiation, through a cascade of actions. The system consists of iron oxide nanoparticles covalently grafted with a thermosensitive alkoxyamine derivative, specifically 6-(4-(1-((di-tert-butylamino)oxy)ethyl) benzamido)hexyl)phosphonic acid. The originality of our approach lies in the unique advantages of alkoxyamines, which offer the ability to generate radicals upon local heating, with tunable activation energy. Additionally, they exhibit significant stability in the absence of external *stimuli* and can be chemically modified, enabling their grafting onto IONPs surfaces. Upon exposure of IONP@alkoxyamine nanoparticles to 340 kHz AMF or 808 nm light irradiation, significant heating occurs at the nanoparticle surface, leading to the homolysis of the thermosensitive C-ON bond in the alkoxyamine and subsequent radical formation in an oxygen-independent manner.

The macroscopic magnetothermal heating of colloidal nanoparticle solutions was investigated, with a view to determining the impact of variables such as nanoparticle concentration, AMF strength and solvent properties on heat transfer. In particular, our findings show that beside well investigated dependence on the concentration of nanoparticles and AMF parameters, the boiling point, viscosity, and specific heat of the solvent significantly influence the heating behaviour during magnetothermal experiments. In addition to magnetothermal activation, we investigated photothermal triggering under 808 nm light irradiation, demonstrating a substantial temperature increase that is dependent on nanoparticle concentration.

The formation of radicals under both external *stimuli* was confirmed using EPR spectroscopy. The kinetics of radical release revealed for the first time that light irradiation at 808 nm (2.6 $W \cdot cm^{-2}$) allowed efficient radical release from grafted nanoparticles at 44 °C ($t_{1/2}$ = 24 min), whereas 20 h are needed for free alkoxyamine to achieve the same conversion at this temperature underscoring the potential for controlled radical release at relatively low temperatures. Moreover, AMF exposure accelerates the homolysis of IONP@alkoxyamine (16 $kA \cdot m^{-1}$, 2.9 $mgmL^{-1}$) twofold compared to the free alkoxyamine at 77 °C ($t_{1/2}$ = 9 min *vs* 18 min).

Importantly, this study demonstrated that the homolysis rate at the surface of the nanoparticles under external *stimuli* is significantly higher than expected based on bulk heating alone. This pronounced difference underscores the importance of nanoscale effects, which could arise from either very localized heating in the corona of the nanoparticle surface or catalytic processes triggered by alternating magnetic field (AMF) or light irradiation. Notably, homolysis of the alkoxyamine did not occur

View Article Online
DOI: 10.1039/D4QM01022A

in the absence of nanoparticles when free alkoxyamines were subjected to external stimuli. The efficient radical generation observed during both AMF and laser irradiation indicates that these nanoscale interactions play a critical role in enhancing the reaction rates of the thermosensitive alkoxyamines, with this effect being much more pronounced under light irradiation.

The results suggest that the IONP@alkoxyamine system not only provides a platform for controlled radical release but also highlights the potential for leveraging nanoscale phenomena to optimize radical generation in various applications. By harnessing the unique thermal and catalytic properties of this system, we can achieve efficient radical release under mild conditions, making it particularly promising for diverse applications. Future investigations will aim to further elucidate the mechanisms driving these nanoscale effects, ultimately enhancing the capabilities of this innovative nanomaterial system.

Author contributions

Conceptualization, G.A., S.M., J.L. and Y.G.; methodology, G.A., S.M., J.L. and G.F.; software, G.F.; validation, S.S., F.A.S. B. B., P.J. and E.A.; investigation, F.A.S., S.S., B.B and J.H. resources, G.A., S.M., J.L, Y.G..; data curation, F.A.S., B.B. and E.A., J.-P.J., E.O.; writing—original draft preparation, J.L., G.F., F.A.S.; writing—review and editing, A.G., S.M., J.L., F.A.S., G.F. and Y.G.; visualization, S.S., G.F., B.B. and J.H.; supervision, S.S., G.F., A.G., S.M., J.-P.J., J.L. and Y.G.; project administration, A.G., S.M., J.L. and Y.G.; funding acquisition, A.G., S.M., J.L. and Y.G.

Conflicts of interest

There are no conflicts to declare.

Data availability

All relevant data are included in this article and its supplementary information files.

Acknowledgements

The authors thank the University of Montpellier, the University of Aix Marseille and CNRS for financial support. The work was developed within the scope of the ANR projects Killer (ANR-22-CE09-0026) , the authors are grateful for funding. Authors are grateful to Platform of Analysis and Characterization (UAR2041) for magnetic, EPR and X-Ray diffraction measurements.

Notes and references

1 M. Moros, J. Idiago-López, L. Asín, E. Moreno-Antolín, L. Beola, V. Grazú, R. M. Fratila, L. Gutiérrez and J. M. de la Fuente, Triggering antitumoural drug release and gene expression by magnetic hyperthermia, *Advanced Drug Delivery Reviews*, 2019, **138**, 326–343.

2 J. F. Liu, B. Jang, D. Issadore and A. Tsourkas, Use of magnetic fields and nanoparticles to trigger drug release and improve tumor targeting, *Wiley Interdiscip Rev Nanomed Nanobiotechnol*, 2019, **11**, e1571.

3 J. Chen, Y. Zhu, C. Wu and J. Shi, Nanoplatform-based cascade engineering for cancer therapy, *Chem. Soc. Rev.*, 2020, **49**, 9057–9094.

4 S. Mura, J. Nicolas and P. Couvreur, Stimuli-responsive nanocarriers for drug delivery, *Nature Mater*, 2013, **12**, 991–1003.

5 S. Su and P. M. Kang, Recent Advances in Nanocarrier-Assisted Therapeutics Delivery Systems, *Pharmaceutics*, 2020, **12**, 837.

6 Y. Zhang, Y. Wang, Q. Zhou, X. Chen, W. Jiao, G. Li, M. Peng, X. Liu, Y. He and H. Fan, Precise Regulation of Enzyme–Nanozyme Cascade Reaction Kinetics by Magnetic Actuation toward Efficient Tumor Therapy, *ACS Appl. Mater. Interfaces*, 2021, **13**, 52395–52405.

7 R. Jauregui, S. Srinivasan, L. N. Vojtech, H. S. Gammill, D. T. Chiu, F. Hladik, P. S. Stayton and J. J. Lai, Temperature-Responsive Magnetic Nanoparticles for Enabling Affinity Separation of Extracellular Vesicles, *ACS Appl. Mater. Interfaces*, 2018, **10**, 33847–33856.

8 Q. M. Kainz and O. Reiser, Polymer- and Dendrimer-Coated Magnetic Nanoparticles as Versatile Supports for Catalysts, Scavengers, and Reagents, *Acc. Chem. Res.*, 2014, **47**, 667–677.

9 Y. Lim, S. Noh, T.-H. Shin, J. Lee, D. Lungerich, J.-H. Lee and J. Cheon, Magnetothermally Activated Nanometer-level Modular Functional Group Grafting of Nanoparticles, *Nano Lett.*, 2021, **21**, 3649–3656.

10 J. G. Ovejero, I. Armenia, D. Serantes, S. Veintemillas-Verdaguer, N. Zeballos, F. López-Gallego, C. Grüttner, J. M. de la Fuente, M. del Puerto Morales and V. Grazu, Selective Magnetic Nanoheating: Combining Iron Oxide Nanoparticles for Multi-Hot-Spot Induction and Sequential Regulation, *Nano Lett.*, 2021, **21**, 7213–7220.

11 H. Gavilán, S. K. Avugadda, T. Fernández-Cabada, N. Soni, M. Cassani, B. T. Mai, R. Chantrell and T. Pellegrino, Magnetic nanoparticles and clusters for magnetic hyperthermia: optimizing their heat performance and developing combinatorial therapies to tackle cancer, *Chem. Soc. Rev.*, 2021, **50**, 11614–11667.

12 P. Guardia, A. Riedinger, S. Nitti, G. Pugliese, S. Marras, A. Genovese, M. E. Materia, C. Lefevre, L. Manna and T. Pellegrino, One pot synthesis of

monodisperse water soluble iron oxide nanocrystals with high values of the specific absorption rate, *J. Mater. Chem. B*, 2014, **2**, 4426–4434.

13 G. Salas, J. Camarero, D. Cabrera, H. Takacs, M. Varela, R. Ludwig, H. Dähring, I. Hilger, R. Miranda, M. del P. Morales and F. J. Teran, Modulation of Magnetic Heating via Dipolar Magnetic Interactions in Monodisperse and Crystalline Iron Oxide Nanoparticles, *J. Phys. Chem. C*, 2014, **118**, 19985–19994.

14 J.-P. Fortin, C. Wilhelm, J. Servais, C. Ménager, J.-C. Bacri and F. Gazeau, Size-Sorted Anionic Iron Oxide Nanomagnets as Colloidal Mediators for Magnetic Hyperthermia, *J. Am. Chem. Soc.*, 2007, **129**, 2628–2635.

15 L. Storozhuk, M. O. Besenhard, S. Mourdikoudis, A. P. LaGrow, M. R. Lees, L. D. Tung, A. Gavriilidis and N. T. K. Thanh, Stable Iron Oxide Nanoflowers with Exceptional Magnetic Heating Efficiency: Simple and Fast Polyol Synthesis, *ACS Appl. Mater. Interfaces*, 2021, **13**, 45870–45880.

16 E. R. Aluri, S. D. Shingte, E. P. McKiernan, S. Ferguson and D. F. Brougham, Modulation of hyperthermic and relaxometric responses of magnetic iron oxide nanoparticles through ligand exchange provides design criteria for dual-functionality, *J. Mater. Chem. C*, 2023, **11**, 6417–6428.

17 A. V. de Walle, A. Figuerola, A. Espinosa, A. Abou-Hassan, M. Estrader and C. Wilhelm, Emergence of magnetic nanoparticles in photothermal and ferroptotic therapies, *Mater. Horiz.*, 2023, **10**, 4757–4775.

18 A. G. Roca, J. F. Lopez-Barbera, A. Lafuente, F. Özel, E. Fantechi, J. Muro-Cruces, M. Hémadi, B. Sepulveda and J. Nogues, Iron oxide nanoparticles (Fe3O4, γ-Fe2O3 and FeO) as photothermal heat mediators in the first, second and third biological windows, *Physics Reports*, 2023, **1043**, 1–35.

19 A. Turki Jalil, M. A. Abdulhadi, L. R. Al-Ameer, O. F. Washeel, S. J. Abdulameer, M. S. Merza, M. Abosaooda and A. A. Mahdi, Free radical based nano cancer therapy, *Journal of Drug Delivery Science and Technology*, 2023, **87**, 104803.

20 J. Liu, B. Jia, Z. Li and W. Li, Reactive oxygen species-responsive polymer drug delivery systems, *Front. Bioeng. Biotechnol.*, 2023, **11**, 1115603.

21 R. S. Chasara, T. O. Ajayi, D. M. Leshilo, M. S. Poka and B. A. Witika, Exploring novel strategies to improve anti-tumour efficiency: The potential for targeting reactive oxygen species, *Heliyon*, 2023, **9**, e19896.

22 M. Overchuk, R. A. Weersink, B. C. Wilson and G. Zheng, Photodynamic and Photothermal Therapies: Synergy Opportunities for Nanomedicine, *ACS Nano*, 2023, **17**, 7979–8003.

23 S. Shi, L. Zhang, M. Zhu, G. Wan, C. Li, J. Zhang, Y. Wang and Y. Wang, Reactive Oxygen Species-Responsive Nanoparticles Based on PEGlated Prodrug for Targeted Treatment of Oral Tongue Squamous Cell Carcinoma by Combining Photodynamic Therapy and Chemotherapy, *ACS Appl. Mater. Interfaces*, 2018, **10**, 29260–29272.

24 O. Guselnikova, S. R. A. Marque, E. V. Tretyakov, D. Mares, V. Jerabek, G. Audran, J.-P. Joly, M. Trusova, V. Svorcik, O. Lyutakov and P. Postnikov, Unprecedented plasmon-induced nitroxide-mediated polymerization (PI-NMP): a method for preparation of functional surfaces, *J. Mater. Chem. A*, 2019, **7**, 12414–12419.

25 X. Meng, L. Li, Y. Huang, X. Deng, X. Liu and Z. Li, Upconversion nanoparticle-assisted cationic and radical/cationic hybrid photopolymerization using sulfonium salts, *Polym. Chem.*, 2021, **12**, 7005–7009.

26 W. Zhou, M. Du, J. Wang, X. Zhang, T. Liang, C. Xie and Q. Fan, Organic nanomaterials for near-infrared light-triggered photothermal/thermodynamic combination therapy, *Dyes and Pigments*, 2022, **205**, 110499.

27 J. Xiao, H. Cong, S. Wang, B. Yu and Y. Shen, Recent research progress in the construction of active free radical nanoreactors and their applications in photodynamic therapy, *Biomater. Sci.*, 2021, **9**, 2384–2412.

28 G. Huang, Y. Qiu, F. Yang, J. Xie, X. Chen, L. Wang and H. Yang, Magnetothermally Triggered Free-Radical Generation for Deep-Seated Tumor Treatment, *Nano Lett.*, 2021, **21**, 2926–2931.

29 H. Hu, X. Deng, Q. Song, W. Yang, Y. Zhang, W. Liu, S. Wang, Z. Liang, X. Xing, J. Zhu, J. Zhang, Z. Shao, B. Wang and Y. Zhang, Mitochondria-targeted accumulation of oxygen-irrelevant free radicals for enhanced synergistic low-temperature photothermal and thermodynamic therapy, *Journal of Nanobiotechnology*, 2021, **19**, 390.

30 X. Li, Y. Liu, F. Fu, M. Cheng, Y. Liu, L. Yu, W. Wang, Y. Wan and Z. Yuan, Single NIR Laser-Activated Multifunctional Nanoparticles for Cascaded Photothermal and Oxygen-Independent Photodynamic Therapy, *Nano-Micro Lett.*, 2019, **11**, 68.

31 D. Ding, Z. Mei, H. Huang, W. Feng, L. Chen, Y. Chen and J. Zhou, Oxygen-Independent Sulfate Radical for

View Article Online
DOI: 10.1039/D4QM01023A

Stimuli-Responsive Tumor Nanotherapy, *Advanced Science*, 2022, **9**, 2200974.

32 J. Yang, R. Xie, L. Feng, B. Liu, R. Lv, C. Li, S. Gai, F. He, P. Yang and J. Lin, Hyperthermia and Controllable Free Radical Coenhanced Synergistic Therapy in Hypoxia Enabled by Near-Infrared-II Light Irradiation, *ACS Nano*, 2019, **13**, 13144–13160.

33 S. Ning, Z. Liu, M. Chen, D. Zhu and Q. Huang, Nanozyme hydrogel for enhanced alkyl radical generation and potent antitumor therapy, *Nanoscale Adv.*, 2022, **4**, 3950–3956.

34 E. Ximendes, R. Marin, Y. Shen, D. Ruiz, D. Gómez-Cerezo, P. Rodríguez-Sevilla, J. Lifante, P. X. Viveros-Méndez, F. Gámez, D. García-Soriano, G. Salas, C. Zalbidea, A. Espinosa, A. Benayas, N. García-Carrillo, L. Cussó, M. Desco, F. J. Teran, B. H. Juárez and D. Jaque, Infrared-Emitting Multimodal Nanostructures for Controlled In Vivo Magnetic Hyperthermia, *Advanced Materials*, 2021, **33**, 2100077.

35 K. El-Boubbou, E. Ximendes, F. J. Teran, R. Marin, Á. Artiga, D. H. Ortgies and D. Jaque, PEGylated Opto-Magnetic Gold and Silver Sulfide Iron Oxide Nanoprobes for Synergistic Photothermal Therapy, *ACS Appl. Nano Mater.*, 2024, **7**, 13959–13972.

36 L. Feng, S. Gai, Y. Dai, F. He, C. Sun, P. Yang, R. Lv, N. Niu, G. An and J. Lin, Controllable Generation of Free Radicals from Multifunctional Heat-Responsive Nanoplatform for Targeted Cancer Therapy, *Chem. Mater.*, 2018, **30**, 526–539.

37 H. Xiang, H. Lin, L. Yu and Y. Chen, Hypoxia-Irrelevant Photonic Thermodynamic Cancer Nanomedicine, *ACS Nano*, 2019, **13**, 2223–2235.

38 X.-Q. Wang, F. Gao and X.-Z. Zhang, Initiator-Loaded Gold Nanocages as a Light-Induced Free-Radical Generator for Cancer Therapy, *Angewandte Chemie International Edition*, 2017, **56**, 9029–9033.

39 F. Wang, Z. Sun, Z. Wang, J. Zhou and L. Sun, PdAu-based nanotheranostic agent for photothermally initiated and oxygen-independent free radical generation, *CrystEngComm*, 2022, **24**, 5090–5096.

40 D. Cao, H. He, W. Li, J. Yan, J. Wu, M. Yin, Y. Zhou, Z. Zhou and L. Yin, A near-infrared light-controlled, oxygen-independent radical generating nano-system toward cancer therapy, *Biomater Sci*, 2021, **9**, 4054–4065.

41 S. Li, M. Qi, Q. Yang, F. Shi, C. Liu, J. Du, Y. Sun, C. Li and B. Dong, State-of-the-Art on the Sulfate Radical-Advanced Oxidation Coupled with Nanomaterials: Biological and Environmental Applications, *Journal of Functional Biomaterials*, 2022, **13**, 227.

42 W. Li, B. Li, B. Wu, B. Tian, X. Chen, C. Wang, W. Hong and J. Peng, Free-Radical Cascade Generated by AIPH/Fe3O4-Coloaded Nanoparticles Enhances MRI-Guided Chemo/Thermodynamic Hypoxic Tumor Therapy, *ACS Appl. Mater. Interfaces*, 2022, **14**, 29563–29576.

43 G. Audran, S. R. A. Marque and P. Mellet, Smart Alkoxyamines: A New Tool for Smart Applications, *Acc. Chem. Res.*, 2020, **53**, 2828–2840.

44 P. Brémond, A. Koïta, S. R. A. Marque, V. Pesce, V. Roubaud and D. Siri, Chemically Triggered C–ON Bond Homolysis of Alkoxyamines. Quaternization of the Alkyl Fragment, *Org. Lett.*, 2012, **14**, 358–361.

45 G. Audran, E. G. Bagryanskaya, S. R. A. Marque and P. Postnikov, New Variants of Nitroxide Mediated Polymerization, *Polymers*, 2020, **12**, 1481.

46 M. Edeleva, G. Audran, S. Marque and E. Bagryanskaya, Smart Control of Nitroxide-Mediated Polymerization Initiators' Reactivity by pH, Complexation with Metals, and Chemical Transformations, *Materials*, 2019, **12**, 688.

47 D. Bertin, D. Gigmes, S. R. A. Marque and P. Tordo, Kinetic subtleties of nitroxide mediated polymerization, *Chem. Soc. Rev.*, 2011, **40**, 2189–2198.

48 B. Bouvet, S. Sene, G. Félix, J. Havot, G. Audran, S. R. A. Marque, J. Larionova and Y. Guari, Cascade strategy for triggered radical release by magnetic nanoparticles grafted with thermosensitive alkoxyamine, *Nanoscale*, 2022, **15**, 144–153.

49 A. Lak, D. Niculaes, G. C. Anyfantis, G. Bertoni, M. J. Barthel, S. Marras, M. Cassani, S. Nitti, A. Athanassiou, C. Giannini and T. Pellegrino, Facile transformation of FeO/Fe3O4 core-shell nanocubes to Fe3O4 via magnetic stimulation, *Sci Rep*, 2016, **6**, 33295.

50 B. Leszczyński, G. C. Hadjipanayis, A. A. El-Gendy, K. Załęski, Z. Śniadecki, A. Musiał, M. Jarek, S. Jurga and A. Skumiel, The influence of oxidation process on exchange bias in egg-shaped FeO/Fe3O4 core/shell nanoparticles, *Journal of Magnetism and Magnetic Materials*, 2016, **416**, 269–274.

51 X. Sun, N. Frey Huls, A. Sigdel and S. Sun, Tuning Exchange Bias in Core/Shell FeO/Fe3O4 Nanoparticles, *Nano Lett.*, 2012, **12**, 246–251.

52 X. Batlle, N. Pérez, P. Guardia, O. Iglesias, A. Labarta, F. Bartolomé, L. M. García, J. Bartolomé, A. G. Roca, M. P. Morales and C. J. Serna, Magnetic nanoparticles with bulklike properties (invited), *Journal of Applied Physics*, 2011, **109**, 07B524.

View Article Online
DOI: 10.1039/D4QM01022A

53 K. Jiang, Q. Zhang, D. T. Hinojosa, L. Zhang, Z. Xiao, Y. Yin, S. Tong, V. L. Colvin and G. Bao, Controlled oxidation and surface modification increase heating capacity of magnetic iron oxide nanoparticles, *Applied Physics Reviews*, 2021, **8**, 031407.

54 A. Espinosa, R. Di Corato, J. Kolosnjaj-Tabi, P. Flaud, T. Pellegrino and C. Wilhelm, Duality of Iron Oxide Nanoparticles in Cancer Therapy: Amplification of Heating Efficiency by Magnetic Hyperthermia and Photothermal Bimodal Treatment, *ACS Nano*, 2016, **10**, 2436–2446.

55 R. R. Wildeboer, P. Southern and Q. A. Pankhurst, On the reliable measurement of specific absorption rates and intrinsic loss parameters in magnetic hyperthermia materials, *J. Phys. D: Appl. Phys.*, 2014, **47**, 495003.

56 O. L. Lanier, O. I. Korotych, A. G. Monsalve, D. Wable, S. Savliwala, N. W. F. Grooms, C. Nacea, O. R. Tuitt and J. Dobson, Evaluation of magnetic nanoparticles for magnetic fluid hyperthermia, *Int J Hyperthermia*, 2019, **36**, 687–701.

57 Z. J. Díaz-Puerto, Á. Raya-Barón, P. W. N. M. van Leeuwen, J. M. Asensio and B. Chaudret, Determination of the surface temperature of magnetically heated nanoparticles using a catalytic approach, *Nanoscale*, 2021, **13**, 12438–12442.

58 M. Vassallo, D. Martella, G. Barrera, F. Celegato, M. Coïsson, R. Ferrero, E. S. Olivetti, A. Troia, H. Sözeri, C. Parmeggiani, D. S. Wiersma, P. Tiberto and A. Manzin, Improvement of Hyperthermia Properties of Iron Oxide Nanoparticles by Surface Coating, *ACS Omega*, 2023, **8**, 2143–2154.

59 O. M. Lemine, N. Madkhali, M. Alshammari, S. Algessair, A. Gismelseed, L. El Mir, M. Hjiri, A. A. Yousif and K. El-Boubbou, Maghemite (γ-Fe2O3) and γ-Fe2O3-TiO2 Nanoparticles for Magnetic Hyperthermia Applications: Synthesis, Characterization and Heating Efficiency, *Materials*, 2021, **14**, 5691.

60 D. Serantes, K. Simeonidis, M. Angelakeris, O. Chubykalo-Fesenko, M. Marciello, M. del P. Morales, D. Baldomir and C. Martinez-Boubeta, Multiplying Magnetic Hyperthermia Response by Nanoparticle Assembling, *J. Phys. Chem. C*, 2014, **118**, 5927–5934.

61 D. Cabrera, J. Camarero, D. Ortega and F. J. Teran, Influence of the aggregation, concentration, and viscosity on the nanomagnetism of iron oxide nanoparticle colloids for magnetic hyperthermia, *J Nanopart Res*, 2015, **17**, 121.

62 A. Rousseau, M. Tellier, L. Marin, M. Garrow, C. Madelaine, N. Hallali and J. Carrey, Influence of medium viscosity on the heating power and the high-frequency magnetic properties of nanobeads containing magnetic nanoparticles, *Journal of Magnetism and Magnetic Materials*, 2021, **518**, 167403.

63 M. E. Sadat, M. Kaveh Baghbador, A. W. Dunn, H. P. Wagner, R. C. Ewing, J. Zhang, H. Xu, G. M. Pauletti, D. B. Mast and D. Shi, Photoluminescence and photothermal effect of Fe3O4 nanoparticles for medical imaging and therapy, *Applied Physics Letters*, 2014, **105**, 091903.

64 A. Espinosa, J. Kolosnjaj-Tabi, A. Abou-Hassan, A. Plan Sangnier, A. Curcio, A. K. A. Silva, R. Di Corato, S. Neveu, T. Pellegrino, L. M. Liz-Marzán and C. Wilhelm, Magnetic (Hyper)Thermia or Photothermia? Progressive Comparison of Iron Oxide and Gold Nanoparticles Heating in Water, in Cells, and In Vivo, *Advanced Functional Materials*, 2018, **28**, 1803660.

65 S. Cabana, A. Curcio, A. Michel, C. Wilhelm and A. Abou-Hassan, Iron Oxide Mediated Photothermal Therapy in the Second Biological Window: A Comparative Study between Magnetite/Maghemite Nanospheres and Nanoflowers, *Nanomaterials*, 2020, **10**, 1548.

66 C. Lozano-Pedraza, E. Plaza-Mayoral, A. Espinosa, B. Sot, A. Serrano, G. Salas, C. Blanco-Andujar, G. Cotin, D. Felder-Flesch, S. Begin-Colin and F. J. Teran, Assessing the parameters modulating optical losses of iron oxide nanoparticles under near infrared irradiation, *Nanoscale Adv.*, 2021, **3**, 6490–6502.

67 S. Marque, Influence of the Nitroxide Structure on the Homolysis Rate Constant of Alkoxyamines: A Taft−Ingold Analysis, *J. Org. Chem.*, 2003, **68**, 7582–7590.

68 J. Marbaix, N. Mille, L.-M. Lacroix, J. M. Asensio, P.-F. Fazzini, K. Soulantica, J. Carrey and B. Chaudret, Tuning the Composition of FeCo Nanoparticle Heating Agents for Magnetically Induced Catalysis, *ACS Appl. Nano Mater.*, 2020, **3**, 3767–3778.

69 E. Cazares-Cortes, S. Cabana, C. Boitard, E. Nehlig, N. Griffete, J. Fresnais, C. Wilhelm, A. Abou-Hassan and C. Ménager, Recent insights in magnetic hyperthermia: From the 'hot-spot' effect for local delivery to combined magneto-photo-thermia using magneto-plasmonic hybrids, *Adv Drug Deliv Rev*, 2019, **138**, 233–246.

70 J. Dong and J. I. Zink, Taking the Temperature of the Interiors of Magnetically Heated Nanoparticles, *ACS Nano*, 2014, **8**, 5199–5207.

71 H. Huang, S. Delikanli, H. Zeng, D. M. Ferkey and A. Pralle, Remote control of ion channels and neurons

through magnetic-field heating of nanoparticles, *Nature Nanotech*, 2010, **5**, 602–606.

72 A. Riedinger, P. Guardia, A. Curcio, M. A. Garcia, R. Cingolani, L. Manna and T. Pellegrino, Subnanometer Local Temperature Probing and Remotely Controlled Drug Release Based on Azo-Functionalized Iron Oxide Nanoparticles, *Nano Lett.*, 2013, **13**, 2399–2406.

73 D. Liu, Y. Huang, J. Hu, B. Wang and Y. Lu, Multiscale Catalysis Under Magnetic Fields: Methodologies, Advances, and Trends, *ChemCatChem*, 2022, **14**, e202200889.

74 O. Guselnikova, G. Audran, J.-P. Joly, A. Trelin, E. V. Tretyakov, V. Svorcik, O. Lyutakov, S. R. A. Marque and P. Postnikov, Establishing plasmon contribution to chemical reactions: alkoxyamines as a thermal probe, *Chem. Sci.*, 2021, **12**, 4154–4161.

75 W. W. Yu, J. C. Falkner, C. T. Yavuz and V. L. Colvin, Synthesis of monodisperse iron oxide nanocrystals by thermal decomposition of iron carboxylate salts, *Chem. Commun.*, 2004, 2306–2307.

76 COMSOL Multiphysics® v. 6.0. www.comsol.com. COMSOL AB, Stockholm, Sweden.

View Article Online
DOI: 10.1039/D4QM01022A

View Article Online
DOI: 10.1039/D4QM01022A

DATA AVAILABILITY STATEMENT

Controlled Radical Release with Iron Oxide Nanoparticles Grafted with Thermosensitive Alkoxyamine Triggered by External Stimuli

Farah Abdel Sater, Basile Bouvet, Saad Sene, Gautier Félix, Erwan Adriaenssens, Jean-Patrick Joly, Gerard Audran, Sylvain R. A. Marque, Joulia Larionova and Yannick Guari

All data generated or analyzed during this study are included in the main article or in the supplementary information files accompanying this article. Additional details and data that support the findings of this study are available from the corresponding author upon reasonable request.

For further information, please contact Pr. Joulia Larionova at joulia.larionova@umontpellier.fr and/or Pr. Sylvain Marque at sylvain.marque@univ-amu.fr.

Pr. G. Audran

Pr. S. R. A. Marque

Pr. J. Larionova